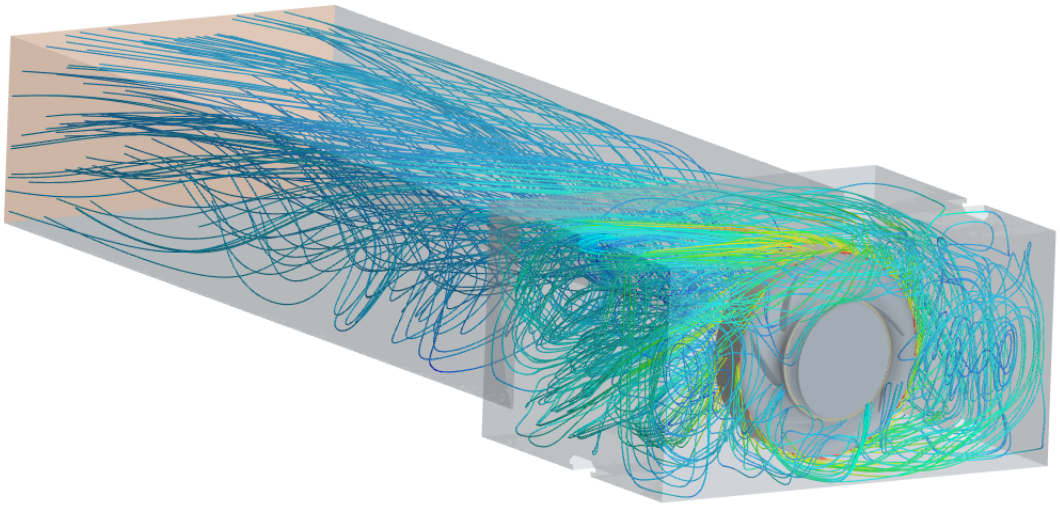

How the distance between the fan outlet and the surrounding walls affects the fan efficiency

An Investigation of the Influence of Outlet-Wall Distance on Fan Efficiency using Computational Fluid Dynamics

Master's thesis in Applied Mechanics and Sustainable Energy Systems

ROBIN BÖHME
LUCAS KALLENBERG

DEPARTMENT OF MECHANICS AND MARITIME SCIENCES

CHALMERS UNIVERSITY OF TECHNOLOGY
Gothenburg, Sweden 2025
www.chalmers.se

Master's Thesis in Applied Mechanics and Sustainable Energy Systems

How the Distance Between the Fan Outlet and the Surrounding Walls Affects Fan Efficiency

A Investigation of the Influence of Outlet-Wall Distance on Fan Efficiency using Computational Fluid Dynamics

ROBIN BÖHME
LUCAS KALLENBERG

CHALMERS
UNIVERSITY OF TECHNOLOGY

Department of Mechanics and Maritime Sciences
Division of Fluid Dynamics
Chalmers University of Technology
Gothenburg, Sweden 2025

How the distance between the fan outlet and the surrounding walls affects the fan efficiency
A Investigation of the Influence of Outlet-Wall Distance on Fan Efficiency using Computational Fluid Dynamics
ROBIN BÖHME
LUCAS KALLENBERG

Supervisor: Martin Ottersten, Swegon Group AB
Examiner: Lars Davidson, Mechanics and Maritime Sciences

Master's Thesis 2025
Department of Mechanics and Maritime Sciences
Chalmers University of Technology
SE-412 96 Gothenburg
Sweden
Telephone +46 31 772 1000

Cover: Airflow visualization constructed in Star-CCM+ using streamlines and velocity magnitude scalar.

Typeset in LaTeX
Gothenburg, Sweden 2025

How the distance between the fan outlet and the surrounding walls affects the fan efficiency
A Investigation of the Influence of Outlet-Wall Distance on Fan Efficiency using Computational Fluid Dynamics
ROBIN BÖHME
LUCAS KALLENBERG
Department of Mechanics and Maritime Sciences
Division of Fluid Dynamics
Chalmers University of Technology

Abstract

This thesis investigates the influence of the outlet-wall distance on the aerodynamic performance of centrifugal fans used in Air Handling Units (AHUs). The study was conducted using steady-state Computational Fluid Dynamics (CFD) simulations with a realizable k–ε turbulence model and Moving Reference Frame (MRF) methodology. The aim was to identify how variations in the height, width, and depth of the outlet enclosure affect fan efficiency and static pressure rise.
A mesh independence study was first carried out to ensure result validity, followed by a systematic variation of outlet geometry. Results showed that increasing the outlet enclosure dimensions led to improved flow uniformity, reduced turbulence, and enhanced fan efficiency. However, the improvements diminished beyond a certain geometric threshold, indicating an optimal enclosure size for performance. Additional modifications such as cone extensions, cylindrical blockages, and rounded corners were also tested and showed further performance gains.
The results offer design guidance for optimizing outlet-wall distances in space-constrained AHU systems. While the findings are based on numerical simulations, they lay the groundwork for future experimental validation and further CFD studies using transient solvers.

Keywords: Fan efficiency, outlet-wall distance, CFD, HVAC, AHU, MRF, plenum fan, turbulence modeling

Preface

This report presents the outcome of our master's thesis project carried out at the Department of Mechanics and Maritime Sciences at Chalmers University of Technology during the spring of 2025.

Transparency in the Use of AI Tools: In accordance with the requirement for transparency in the use of AI tools, we hereby disclose their role in the preparation of this report. Grammarly and ChatGPT were utilized to enhance the clarity, grammar, and formatting of our own written text and conclusions. These tools were employed exclusively for language refinement and did not contribute to the generation of original content or ideas.

Acknowledgements

We would like to express our sincere gratitude to Swegon Group AB for providing the opportunity to carry out this thesis project and for supplying the geometry, data, and practical insights necessary for the simulations. The collaboration with Swegon made it possible to explore a highly relevant and applied engineering challenge within the field of indoor climate solutions.
We are especially thankful to our industrial supervisor Martin Ottersten at Swegon for his continuous guidance, valuable feedback, and encouragement throughout the course of this project. His technical expertise and insights into real-world HVAC applications have been instrumental to the success of this work.
We would also like to extend our appreciation to our academic examiner, Professor Lars Davidson at the Department of Mechanics and Maritime Sciences, Chalmers University of Technology.

Robin Böhme, Lucas Kallenberg, Gothenburg, June 2025

List of Acronyms

Below is the list of acronyms that have been used throughout this thesis listed in alphabetical order:

AHU	Air Handling Unit
CFD	Computational Fluid Dynamics
HVAC	Heating, Ventilation and Air Conditioning
MRF	Moving Reference Frame
RPM	Revolutions Per Minute
TKE	Turbulent Kinetic Energy

Nomenclature

Below is the nomenclature of indices, sets, parameters, and variables that have been used throughout this thesis.

Symbols

i, j	Tensor indices
x_i	Spatial coordinate in direction i
v_i	Velocity component in direction i

Greek Symbols

ρ	Density of air
u	Internal energy
k	Turbulent kinetic energy
ε	Dissipation rate of turbulent kinetic energy
ν	Kinematic viscosity
μ	Dynamic viscosity
y^+	Dimensionless wall distance
τ_w	Wall shear stress
ν_t	Turbulent viscosity

Fan Performance Variables

Q_{AHU}	Volume flow rate at inlet of Air Handling Unit (AHU)
Δp_s	Static pressure rise across the fan
M_{fan}	Torque generated by the fan
ω	Angular velocity (rad/s)

η_{AHU}	Fan efficiency of the AHU

Energy and Governing Equations

P	Pressure
T	Temperature
q_i	Heat flux vector
σ_{ij}	Stress tensor
τ_{ij}	Viscous stress tensor
S_{ij}	Strain rate tensor

Contents

List of Figures

List of Tables

1
Introduction

1.1 Background

Swegon is a leading company specializing in indoor climate solutions, particularly in the manufacturing of ventilation systems. A key component of these systems is the Air Handling Unit (AHU), which ensures the continuous supply of fresh, conditioned air into buildings. Within the AHU, a centrifugal fan is responsible for air transport, operating within a confined space known as the fan-room. The proximity of the surrounding walls to the fan outlet, defined as the outlet-wall distance, significantly influences the fan's performance and overall system efficiency.

Optimizing this distance is essential to achieving maximum fan efficiency, reducing energy consumption, and improving the overall system. Modern buildings often prioritize compact, space-efficient designs. Therefore, understanding how outlet-wall distances influence airflow and pressure distribution is essential. This knowledge can lead to more efficient AHU designs, lower operational costs, and improved sustainability in building ventilation systems.

1.2 Purpose

The primary purpose of this study is to analyze the effect of outlet-wall distance on fan efficiency in an AHU using Computational Fluid Dynamics (CFD) simulations. Given that space constraints in ventilation systems often require fan-rooms to be as compact as possible, it is important to determine the optimal ratio between fan outlet distance and surrounding walls that minimizes energy losses while maintaining efficient airflow.

By optimizing this parameter, the study aims to contribute to the development of energy efficient ventilation systems, reducing both energy consumption and operational costs.

1.3 Goals

This project aims to achieve the following:

- Investigate and map the impact of the aspect ratios (height, width, depth) on fan performance.

- Analyze how varying these ratios influence internal flow structures.
- If time allows, the effect of new design elements will be explored to enhance performance.

1.4 Limitations and Scope

Due to the nature of the project, the study is subject to the following constraints:

- The study is constrained to Swegon's single-fan AHU design, and other configurations will not be considered.
- The fan type is fixed, meaning no modifications will be made to the fan itself.
- The study focuses mainly on the dimensions of the surrounding walls within the AHU while keeping other design parameters unchanged.
- The primary objective is to analyze fan efficiency, with only a brief consideration of other physical effects.
- The study is limited to the timeframe of 30/01/2025 to 10/06/2025, restricting the extent of possible iterations.
- The computational power is limited to the available school resources.

2
Theory

In the following chapter the theory of different concepts that are used in this work will be presented. The theory is for the reader to get a better understanding of how some of the work has been conducted.

2.1 The Governing Equations

This section presents the fundamental equations governing the behavior of Newtonian viscous fluids. These equations form the basis for fluid dynamics as well as for CFD simulations, and they describe how mass, momentum, and energy are conserved in a fluid domain.

2.1.1 The Continuity Equation

The continuity equation ensures the conservation of mass within a control volume. For incompressible and compressible flow, it expresses the balance between the time rate of change of density and the divergence of mass flux. The continuity equation taken from [1] which is stated in Einstein notation:

$$\dot{\rho} + \rho v_{i,i} = 0 \tag{2.1}$$

The formulation is more commonly seen on the expanded notation form as the one below:

$$\frac{d\rho}{dt} + \rho \frac{\partial v_i}{\partial x_i} = 0 \tag{2.2}$$

For incompressible flows, where the density ρ is constant, the equation simplifies to:

$$\rho \frac{\partial v_i}{\partial x_i} = 0 \tag{2.3}$$

This implies that the net volume flow rate into a differential element is zero, ensuring mass is neither created nor destroyed.

2.1.2 The Momentum Equation

The momentum equation, also known as the Navier-Stokes equation, arises from Newton's second law and governs the conservation of momentum in a fluid. For a Newtonian fluid, the equation is expressed as [1]:

$$\sigma_{ji,j} + \rho f_i = \rho \dot{v}_i \tag{2.4}$$

Rewriting it as [2] the momentum equation is be written as the following terms where σ_{ij} is the stress tensor and τ_{ij} is the viscous stress tensor.

$$\sigma_{ij} = -P\delta_{ij} + 2\mu S_{ij} - \frac{2}{3}\mu S_{kk}\delta_{ij} \tag{2.5}$$

$$\tau_{ij} = 2\mu S_{ij} - \frac{2}{3}\mu S_{kk}\delta_{ij} \tag{2.6}$$

$$\underbrace{\rho\frac{dv_i}{dt}}_{\text{I}} = -\frac{\partial P}{\partial x_i} + \frac{\partial \tau_{ji}}{\partial x_j} + \rho f_i = \underbrace{-\frac{\partial P}{\partial x_i}}_{\text{II}} + \underbrace{\frac{\partial}{\partial x_j}\left(2\mu S_{ij} - \frac{2}{3}\mu\frac{\partial v_k}{\partial x_k}\delta_{ij}\right)}_{\text{III}} + \underbrace{\rho f_i}_{\text{IV}} \tag{2.7}$$

In equation 2.7 the first term I is the material derivative and describes the rate of change and the convective term. Term II is the pressure gradient, term III is the diffusive term and describes the viscous forces. The last term IV is the external force term more often called the body force term.

2.1.3 The Energy Equation

Using the energy equation stated in [1] and rewriting it to the transport equation for total energy from [2].

$$\rho\dot{e} - v_{i,j}\sigma_{ij} + q_{i,i} = \rho z \tag{2.8}$$

The energy equation written is for the sum of internal and kinetic energy, u + k. Where $k = \frac{v_i v_i}{2}$ and the radiation is neglected.

$$\rho\frac{d(u+k)}{dt} = \underbrace{\frac{\partial \sigma_j v_i}{\partial x_j}}_{\text{I}} - \underbrace{\frac{\partial q_i}{\partial x_i}}_{\text{II}} + \rho v_i f_i \tag{2.9}$$

To expand term I, the stress tensor σ_{ij} is expressed as the sum of pressure and viscous stress components, with the viscous stress tensor τ_{ij} defined as in equation 2.6:

$$\sigma_{ji}\frac{\partial v_i}{\partial x_j} = -P\frac{\partial v_i}{\partial x_i} + \tau_{ji}\frac{\partial v_i}{\partial x_j} \tag{2.10}$$

The heat flux vector q_i is defined by Fourier's law as:

$$q_i = -k\frac{\partial T}{\partial x_i} \tag{2.11}$$

The pressure term represents reversible processes of compression and expansion. The viscous term accounts for dissipation, where kinetic energy is irreversibly converted into thermal energy — a key effect in turbulent flows. The heat flux term represents conductive energy transfer due to temperature gradients.

2.2 Turbulence model

2.2.1 $k - \varepsilon$

The $k-\varepsilon$ is a turbulence model used in CFD. This model is based on two transport equations that describe turbulence characteristics. The first equation governs the turbulent kinetic energy, k, which represents the energy in turbulent fluctuations, and the second equation describes the dissipation rate, ε, which describes the rate at which the turbulent kinetic energy is converted into heat. These equations provide means to approximate the effects of turbulent flow without resolving all scales of turbulence [3]. The transport equations for k and ε are given by [4]:

$$\frac{\partial k}{\partial t} + U_j \frac{\partial k}{\partial x_j} = \frac{\partial}{\partial x_j}\left[\left(\nu + \frac{\nu_t}{\sigma_k}\right)\frac{\partial k}{\partial x_j}\right] + P_k - \varepsilon \tag{2.12}$$

$$\frac{\partial \varepsilon}{\partial t} + U_j \frac{\partial \varepsilon}{\partial x_j} = \frac{\partial}{\partial x_j}\left[\left(\nu + \frac{\nu_t}{\sigma_\varepsilon}\right)\frac{\partial \varepsilon}{\partial x_j}\right] + C_1 \frac{\varepsilon}{k} P_k - C_2 \frac{\varepsilon^2}{k} \tag{2.13}$$

where the production of turbulent kinetic energy is defined as [2]:

$$P_k = \nu_t \left(\frac{\partial \bar{v}_i}{\partial x_j} + \frac{\partial \bar{v}_j}{\partial x_i}\right)\frac{\partial \bar{v}_i}{\partial x_j} = 2\nu_t \bar{s}_{ij}\bar{s}_{ij} \tag{2.14}$$

and the turbulent viscosity is modeled as:

$$\nu_t = C_\mu \frac{k^2}{\varepsilon}. \tag{2.15}$$

The standard empirical constants used in the model are:

$$C_\mu = 0.09, \quad C_1 = 1.44, \quad C_2 = 1.92, \quad \sigma_k = 1.0, \quad \sigma_\varepsilon = 1.3. \tag{2.16}$$

The $k-\varepsilon$ model is computationally efficient and performs well for high Reynolds number flows, making it suitable for industrial applications. However, the model performs poorly for flows with flows with lower Reynolds-number and adverse pressure gradients [3].

2.2.2 Turbulent Boundary Layer

In the near-wall region, velocity rapidly decreases from high to zero over a very short distance, resulting in significant velocity gradients. This region of the turbulent boundary layer can be divided into four distinct zones: the viscous sublayer, buffer layer, log-law region, and outer region [5]. The viscous sublayer is closest to the wall, while the outer region is the farthest, as can be seen in Figure 2.1.

By relating the Reynolds number to the wall distance, it is observed that the Reynolds number is high in the outer region and decreases as the wall distance reduces. Eventually, a point is reached where viscous and inertial forces are of equal magnitude. Closer to the wall, viscous forces dominate, leading to a laminar-like

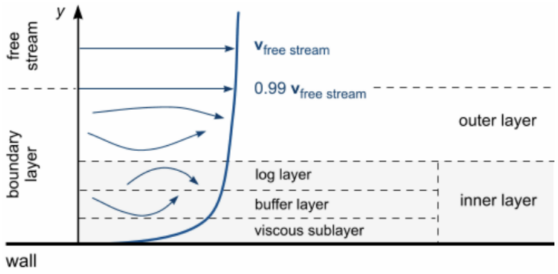

Figure 2.1: Turbulent boundary layer: velocity profile and sub-layers [6]

flow regime [5].

This relationship between the Reynolds number and wall distance allows for defining the dimensionless wall distance, y^+, as [5]:

$$y^+ = \frac{y \cdot u_t}{\nu} \quad u_t = \sqrt{\frac{\tau_w}{\rho}} \quad u^+ = \frac{u}{u_t}$$

where y is the wall distance, u_t is the friction velocity, τ_w is the wall shear stress, ν is the kinematic viscosity, and u is the velocity at the given wall distance.

Using the dimensionless wall distance y^+, the different boundary layer regions can be categorized as follows[5]:

- Viscous sublayer $y^+ < 10$
- Buffer region $5 < y^+ < 30$
- Log-law region $30 < y^+ < 300$
- Outer region $300 < y^+$

2.3 Fan Theory

Fans are used in a wide verity of applications and different purposes. For heat, ventilating and air conditioning (HVAC) systems there are two main type of fans that are used, the axial and centrifugal fan [7]. This study is looking at centrifugal fans that used in AHU that are similar to the GOLD model from Swegon [8], seen down below in Figure 2.2, in a open configuration without a spiral casing which most centrifugal fans have. This type of fan is called plenum fans.

Figure 2.2: Overview of Swegon's air handling unit [9], reproduced with permission from Swegon

2.3.1 Centrifugal Fan Design

A centrifugal fan is composed of three primary components: fan blades, backplate, and shroud. Its construction is illustrated in Figure 2.3(a), where the fan blades is sandwiched between the backplate and shroud. Enhancing efficiency, centrifugal fans often include additional elements, such as an inlet duct and fan housing. Centrifugal fans function by using two principles: first using centrifugal force (hence the name centrifugal fan), which produces higher static pressure compared to axial fans with equal dimensions. Secondly deflection of airflow by the vanes pushing the air. The flow of air that goes axially into the fan and radially out can be seen in Figure 2.3(b).

This study examines the centrifugal plenum fan. Plenum fans are most commonly used in HVAC systems due to their advantages, including flexibility in equipment discharge and the potential for a more compact footprint. Plenum fans eliminate the need for traditional scroll housings, allowing air to exit in multiple directions, which simplifies duct connections and reduces installation complexity.

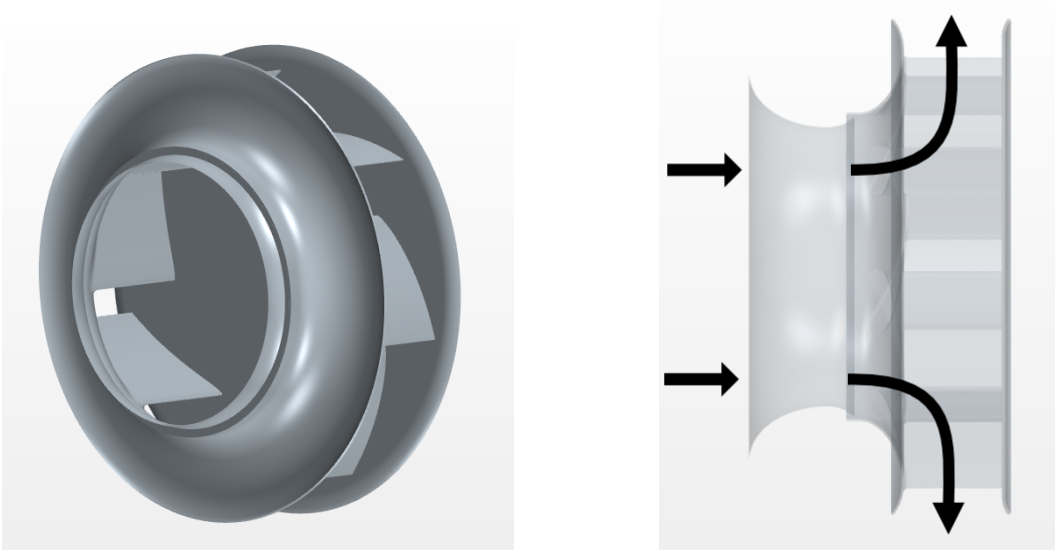

(a) Construction of a centrifugal fan.

(b) The airflow through a plenum fan with a inlet duct.

Figure 2.3: Centrifugal fan with backward curved airfoils.

There are three major types of centrifugal fan blade types, the forward curved (FC), backward curved (BC, BI) and radial/straight (RB) blades, seen in Figure 2.4. There are many variants and designs for each blade typ but the most efficient one is the backward airfoil (AF) design [10], [11]. The curved, backward/inclined design is slightly less efficient, with the forward and radial blade design being the least efficient of the three.

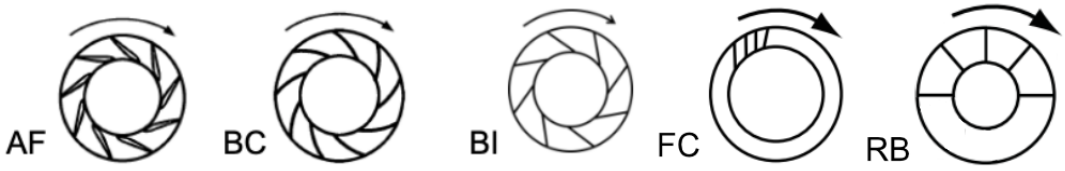

Figure 2.4: Different types of fan blades. Reproduced with permission from AMCA [12].

2.3.2 Fan and System Curves

Fan and system curves are a fundamental tool for understanding the interaction between a fan and the system in which it operates. Fan and system curves help to visualize this by showing how static pressure and volume flowrate relates to each other. The point where these lines meet determines how the system operates and can be helpful for decisions about fan selection and system adjustments.

A fan curve represents the performance for different operating. It describes how the fan performs under different operating conditions by plotting performance parameters such as airflow, static pressure and power consuption for a set rotational speed,

as can be shown in Figure 2.5. where the y-axis shows the generated static pressure and the x-axis shows the fan volume flow rate [13].

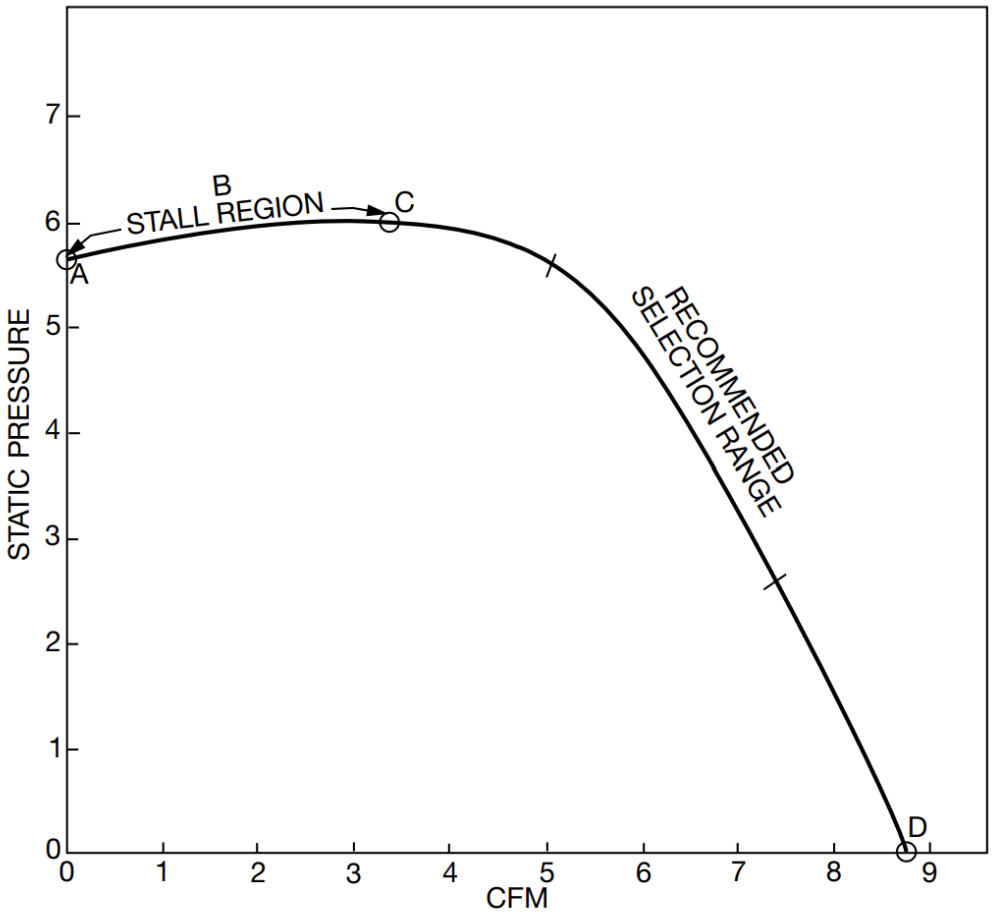

Figure 2.5: Fan curve

A fan curve typically begins at a shut-off point, The condition where the fan produces maximum pressure but no airflow due to system blockage. As airflow increases, the pressure generated by the fan decreases, following a characteristic curve until reaching the free-air delivery point, where the fan moves the maximum volume of air under minimal resistance. The stall region is an unstable operating range that occurs when airflow decreases while pressure remains relatively high. When a fan operates within this region unsteady operation and surging effects may occur, which leads to reduced efficiency and increased wear of the system[13].

The system line represents the relationship between static pressure and volume flow rate within a given system and the shape of the curve is determined by the fan laws. Lastly the power curve describes how much power the fan consumes at different airflow rates. Adding the system line and power curve to Figure 2.5 allows the operating point of the system to be located.

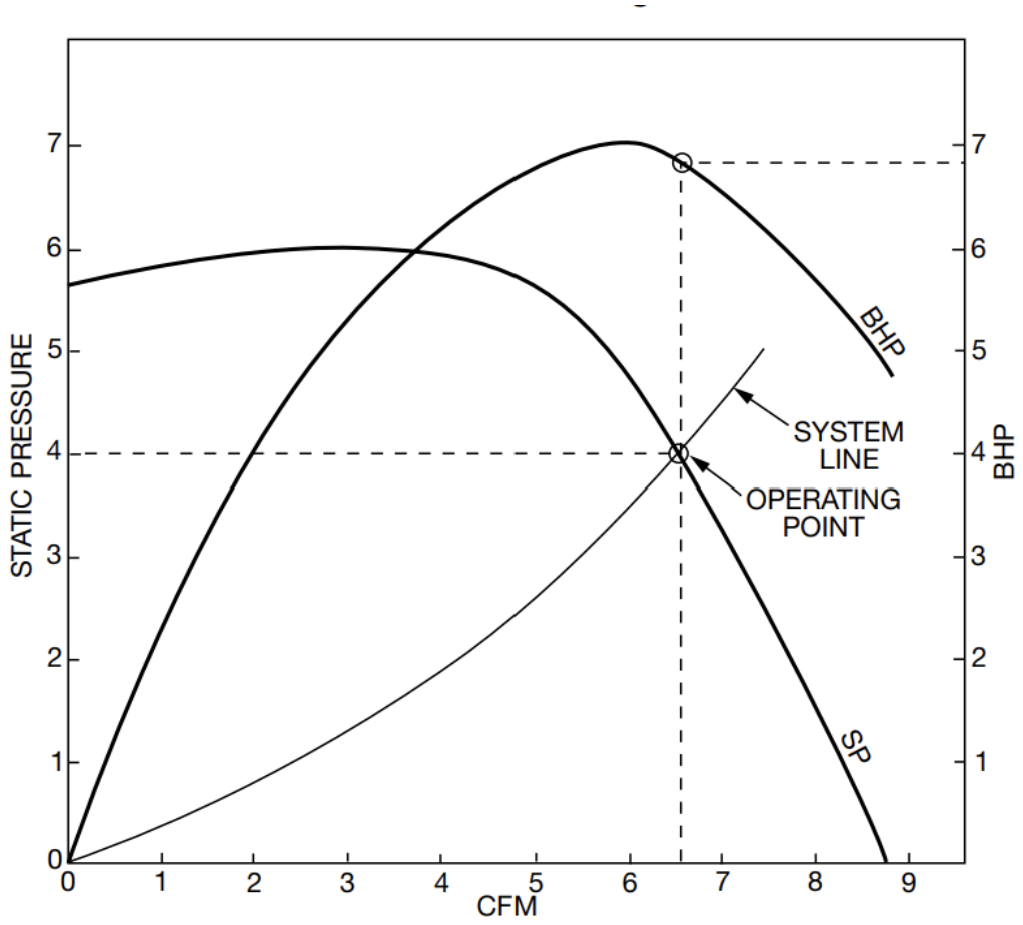

Figure 2.6: Operating point

The operating point of a fan system is the equilibrium point where the fan's pressure rise matches the system's pressure loss at a given airflow rate. The operating point can thus be found where the system line and fan curve intersects, which defines the actual flow rate and static pressure that is delivered by the system. Projecting the point of intersection upward gives the power required for the system[12].

2.3.3 Fan Efficiency

Fan efficiency is determined by the ratio of power transferred to the airflow to the power consumed by the motor to drive the fan, commonly referred to as brake horsepower (BHP). The power delivered to the airflow is calculated by multiplying the difference in static pressure between the inlet and outlet of the AHU with the volume flow rate at the inlet. Meanwhile, brake horsepower is obtained by multiplying the torque produced by the fan with the rotational speed of each individual fan. The efficiency can then be described by the following equation [14]:

$$\eta_{AHU} = \frac{Q_{AHU} \cdot \Delta p_s}{M_{total} \cdot \omega} = \frac{\dot{m}_{inlet}}{\rho_{air}} \cdot \frac{(p_{out} - p_{in})}{M_{fan} \cdot rpm \cdot 2\pi/60} \tag{2.17}$$

2.4 Meshing Strategy

In the following section various meshing strategies and techniques used for generating high quality meshes in rotating fan simulations is discussed. Proper meshing is required to accurately capture the complex flow dynamics and interactions within the fan system. Different approaches, such as boundary layer refinement, moving reference frame (MRF) and the sliding mesh technique are used to improve numerical stability and computational efficiency. The benefits and drawbacks are outlined below.

2.4.1 Meshing Turbulent Boundary Layer

When solving turbulent flow near solid walls, wall functions are used to model the near-wall region without requiring very fine mesh resolution [15]. In the turbulent boundary layer, large velocity and property gradients exist close to the wall, making it necessary to refine the mesh in this region. To accurately resolve these gradients while maintaining computational efficiency, a mesh with prism layers is applied near the surface [3]. These layers consist of cells aligned normal to the wall and allow for a gradual transition to coarser mesh in the outer flow. Wall first cell center within the appropriate dimensionless wall distance range ($30 < y^+ < 300$) [16]. Without prism layers, the mesh near the wall may not capture the necessary gradients, resulting in poor prediction of shear stress and turbulence behavior. Therefore, using prism layers is essential for accurate and stable near-wall turbulence modeling.

2.4.2 Two-Layer Wall Treatment

The two-layer all-y^+ wall treatment is a near-wall turbulence modeling method used to simulate turbulent boundary layers without fully resolving the viscous sublayer. This method is implemented in STAR-CCM+ and divides the near-wall region into two zones: a viscous sublayer close to the wall and a fully turbulent outer region [17]. In the viscous sublayer ($y^+ < 30$), turbulence properties are computed using empirical damping functions, while the outer region applies standard logarithmic wall functions [15]. A blending function ensures a smooth transition between these two regions. The two-layer approach enables accurate predictions of wall-bounded turbulent flows, even in the presence of adverse pressure gradients or mild separation, while maintaining reasonable computational cost. For the model to work effectively, the mesh near the wall must include prism layers to ensure that the first cell lies within the appropriate y^+ range.

2.4.3 Simulation of Rotating Objects

There are two major modeling approaches for modeling rotating fans and turbomachinery. The two models are the MRF which models steady-state calculations and the sliding mesh technique and is used for transient modeling.

2.4.4 Moving Reference Frame

MRF is a widely used steady-state modeling approach for simulating rotating machinery. It separates the computational domain into two regions: a stationary domain and a rotating domain, with each solved using equations formulated in its respective frame of reference [18]. In the stationary region, the standard Navier-Stokes equations are applied, while in the rotating domain, the equations are modified to account for rotational effects. It is important to note that the mesh remains fixed throughout the simulation, which simplifies the numerical implementation by avoiding mesh deformation and significantly reduces computational cost. Because the relative motion between rotating and stationary components is not explicitly modeled over time, the MRF method is commonly referred to as the "frozen rotor approach" [19]. Instead of resolving transient interactions, the method uses interpolation across the interface between rotating and stationary regions to ensure continuity in flow variables. The relative velocity in the rotating frame is defined as:

$$\vec{v}_{\mathrm{MRF}} = \vec{v} - \vec{\omega} \times \vec{r} \tag{2.18}$$

where $\vec{v}$ is the absolute velocity, $\vec{\omega}$ is the angular velocity vector, and $\vec{r}$ is the position vector in the rotating frame [20]. This velocity transformation allows the governing equations to account for centrifugal and Coriolis forces in the rotating domain. While the MRF method does not capture unsteady interactions, it is particularly effective for steady-state simulations of rotating equipment such as fans, pumps, and turbines, where the interaction between rotating blades and stationary components is relatively weak [21],[22].

2.4.5 Sliding Mesh Technique

The sliding mesh technique is used for simulating unsteady rotating flows. The model works by using a single mesh which is sub-divided into a moving and static part and are separated by a sliding interface [23]. When the simulation makes a time step the interfaces detaches and moves at set velocity and then re-attaches and the information from the cells can be transferred. The sliding mesh model is theoretically the most accurate model for transient rotating simulation, but it comes at a higher computational cost [21],[24]. The sliding mesh model is used for rotating machinery and time-dependent processes, such as mixing, turbines, propellers and for start up and shut down sequences.

2.4.6 Skewness Angle

One of the fundamental parameters used to assess mesh quality is the skewness angle. Skewness quantifies the deviation of a mesh element's shape from an ideal configuration, and it is particularly important in the discretization of governing equations, as it directly influences numerical accuracy and convergence behavior.

The skewness angle is a measure of how much a mesh element diverges from an optimal shape. defined based on the angle between the vector connecting two adjacent

cell centers and the vector normal to the shared face between those cells as shown in 2.7. Ideally, these two vectors should align perfectly, resulting in a skewness angle of 0°, which indicates orthogonality. As the misalignment increases, so does the skewness angle.

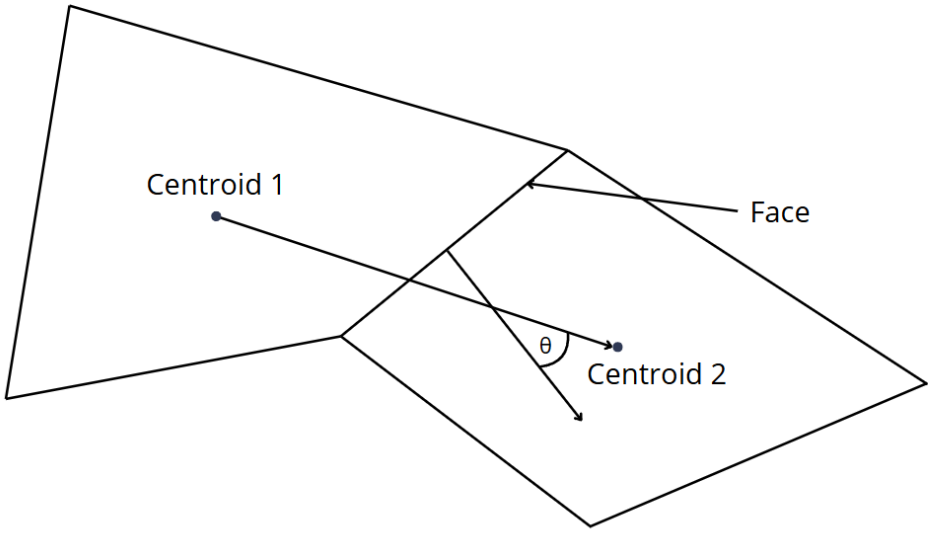

Figure 2.7: Skewness angle

High skewness angles can lead to numerical errors due to increased interpolation errors and poor gradient resolution, especially near walls or in regions with high velocity or pressure gradients. This can adversely affect convergence, lead to non-physical results, and necessitate the use of more diffusive numerical schemes that compromise accuracy.

In CFD, it is generally recommended to avoid skewness angles greater than 85°, as they can introduce numerical instabilities and reduce the overall robustness of the simulation [17]. Skewness angles exceeding 90° are particularly problematic and may lead to critical errors, including convergence issues and inaccurate results.

3
Methods

3.1 Project Structure

The structure of the project is illustrated in the flow chart in Figure 3.1. The work began with a literature review of the relevant topics forming the foundation of this study. Following this, a mesh study was conducted in which the original mesh case provided by Swegon was systematically coarsened. The objective was to achieve mesh independence by evaluating various flow properties, thereby identifying a coarser mesh that still yielded reliable results, ultimately reducing the computational time required for the simulations.

Once a suitable mesh was identified, it served as the basis for subsequent geometry modifications. These modifications enabled the simulation of cases with varying height-to-diameter and width-to-diameter ratios. After completing these simulations, the results were analyzed to identify trends and critical cases. Selected cases were then chosen for further investigation, particularly to study the impact of varying the depth ratio.

Upon completing the primary objective examining how different geometric aspect ratios influence the performance of the AHU additional simulations were carried out. These involved implementing new elements into the original volume to assess their effects. Finally, the results from all simulations were compiled and analyzed to form the basis for the conclusions of this study.

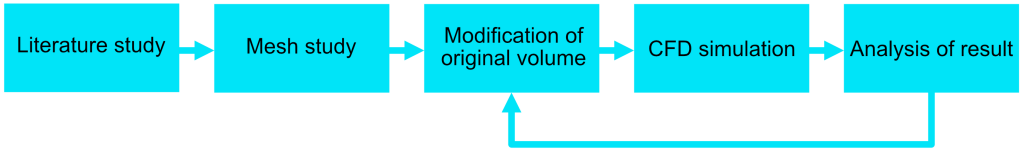

Figure 3.1: Flow chart of project structure

3.2 Geometry and Computational Domain

The geometry and computational domain was given from Swegon in a Star-CCM+ file which can be seen in Figure 3.2. The figure depicts the geometry of a plenum fan along with the fan assembly enclosed within a box representing the volume of a AHU, featuring a cylindrical inlet and a rectangular outlet that simulates ventilation

ducting.

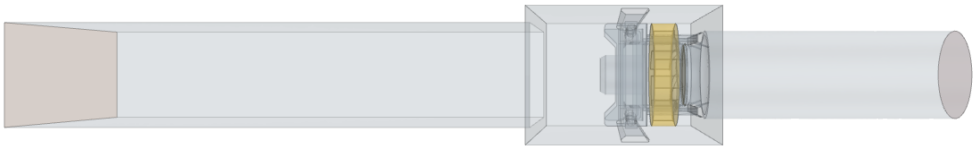

Figure 3.2: A transparent figure of the geometry.

The original geometry feature four blocks connecting the fan assembly to the fan enclosure. A zoomed-in view of one of the blocks is shown in Figure 3.3. These blocks were removed from our simulation geometry in order to simplify the domain and facilitate easier modification of the geometry.

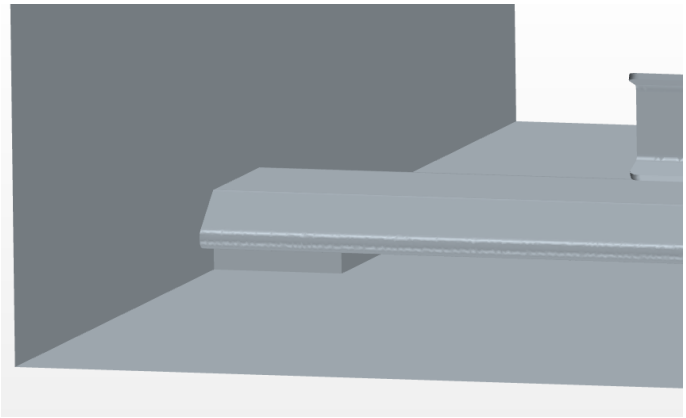

Figure 3.3: Zoomed in view of a connecting block

3.2.1 Regions

The computational domain was divided into three regions, inlet, fan and the outlet which can be seen in Figure 3.4. In Table 3.1 the general measurements of the setup is specified. The diameter of the fan (D_{fan}) is measured from the trailing edge of the blade and the dimension of the outlet is a set Swedish standard (SS) that is used for ventilation.

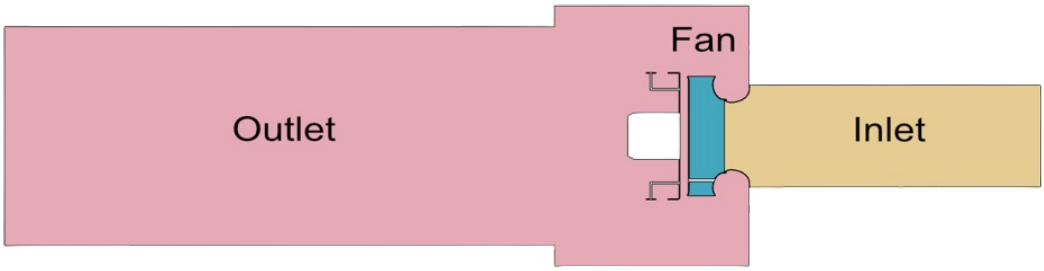

Figure 3.4: The computational domain three regions.

Table 3.1: Dimensions of the geometry

Parameters		**Values**
Inlet diameter	(D_{inlet})	275 mm
Inlet length	(L_{inlet})	800 mm
Outlet width	(W_{outlet})	600 mm
Outlet height	(H_{outlet})	300 mm
Outlet length	(L_{outlet})	1510 mm
Outlet box width	(W_{box})	713 mm
Outlet box height	(H_{box})	377 mm
Outlet box length	(L_{box})	535 mm
Fan diameter	(D_{fan})	293 mm

3.2.1.1 Inlet Region

The inlet region was designed to ensure a uniform and fully developed flow before reaching the fan. It contains the inlet duct, commonly used in plenum fans, and a cylindrical shape duct which was selected to minimize disturbances and provide realistic boundary conditions, reducing the risk of backflow. A sufficient inlet length was maintained to allow the velocity profile to stabilize before interacting with the fan, ensuring accurate and reliable simulations. The Inlet region feature a velocity inlet and a internal interface boundary, connecting the inlet region to the fan region. Both of which can be seen in Figure 3.5.

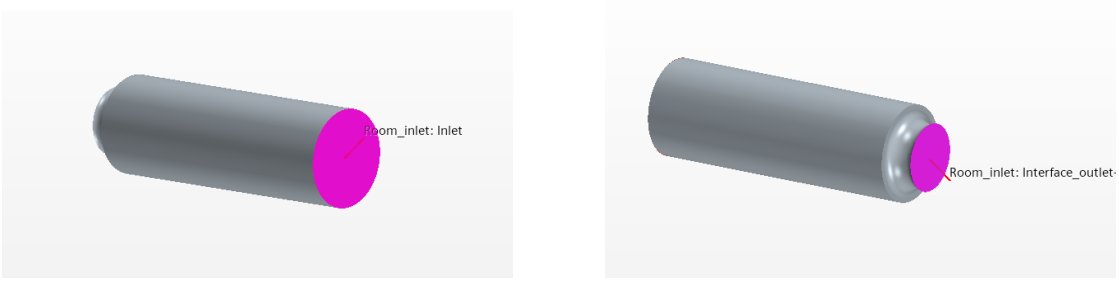

(a) Inlet boundary of the inlet region

(b) Outlet boundary of the inlet region

Figure 3.5: Inlet and outlet boundary of the inlet region

3.2.1.2 Fan Region

To simulate the rotation of the fan MRF was used, treating the fan as rotating reference frame with a constant rotational speed of 3300 rpm, while maintaining a steady-state solution. The fan region comprises a rotating fan with three interfaces that connect the inlet and outlet regions. The fan has two inlets, one from the inlet region (interface 1), the other is from the outlet region (interface 2) and is the gap between the two regions. Then the fans outlet is at interface 3, which in turn is the outlets "inlet". The interfaces can be seen in Figure 3.6.

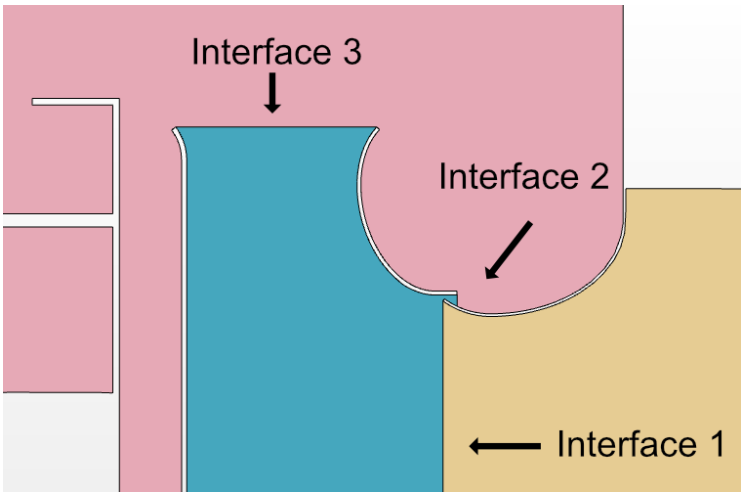

Figure 3.6: Figure of the interfaces that connects the three regions.

3.2.1.3 Outlet Region

The outlet region contains the remaining components of the system, including the fan assembly, the fan housing, and the standardized outlet duct. The fan housing encloses the fan, ensuring controlled airflow, while the outlet duct allows the flow to stabilize before measurements are taken.

This region is connected to the fan region through two internal interfaces: one allowing the airflow to transition from the fan to the outlet region, and another at the outlet region to the fan region at the gap, which allows for recirculating effects to the fan. The outlet of the duct is set as a pressure outlet. Both of which can be seen in Figure 3.7.

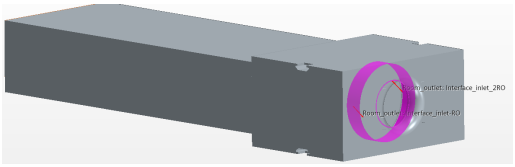

(a) Inlet from the fan region and outlet from the Gap

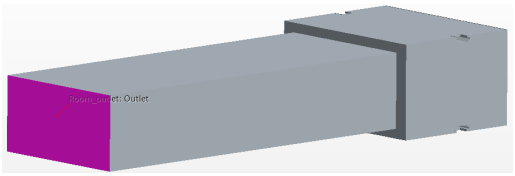

(b) Outlet Boundary

Figure 3.7: Inlet and outlet boundary of the outlet region

3.2.2 Models and Solver Settings

Specifying the models and solver settings was provided by Swegon which follows previous similar works like [25], [26]. After reviewing the physical models and how they were selected, it was found that they followed the Simcenter STAR-CCM+ 2402 User Guide [27] for MRF, and the turbulence models and wall functions was selected automatically with standard values for the realizable K-Epsilon model. For models chosen for K-Epsilon see Table 3.2. The gas used in the model was air with standard values from STAR-CCM+.

Table 3.2: Model set up K-Epsilon

Models
Gas
Gradients
Ideal Gas
K-Epsilon Turbulence
Realizable K-Epsilon Two-Layer
Reynolds-Averaged Navier-Stokes
Segregated Flow
Segregated Fluid Enthalpy
Solution Interpolation
Steady
Three Dimensional
Turbulent
Two-Layer All y+ Wall Treatment
Wall Distance

3.2.3 Boundary Conditions

The boundary conditions have been provided by Swegon based on previous centrifugal fan simulations conducted by the company. For types and values set at the different regions see Table 3.3. The model temperature was set to 300 K, and all walls were defined as no-slip, smooth surfaces with the same logarithmic law offset and Von Kármán constant.

Table 3.3: Boundary conditions

Parameter	**Type**	**Value**
Entire model	Temperature	300K
Walls	No-slip	-
	Smooth	-
	E (Log law offset)	0.9
	κ (*Von Kármán constant*)	0.42
Inlet	Velocity	11 m/s
	Turbulent intensity	0.04
	Turbulent viscosity ratio	10
Outlet	Pressure outlet	1 atm
	Turbulent intensity	0.45
	Turbulent viscosity ratio	10
Fan	Rotating	
	Rotation	3300 rpm

3.3 Meshing and Independence Study

For the mesh an initial working mesh, provided by Swegon, was used as a starting point. The meshing was divided into three regions, and imprinting was applied to align surfaces and match cells. All three regions used polyhedral cells, prism layers, surface remesher and automatic surface repair. In all regions, surfaces were divided, and custom controls were applied to adjust cell sizes for accurately capturing flow features.

Mesh quality was evaluated following the application of the surface remesher and automatic surface repair tools. The minimum face quality thresholds were set to 0.2 for the surface remesher and 0.1 for the automatic surface repair. Assessed mesh quality parameters included face validity, cell quality, cell skewness angle, and volume change. Acceptable ranges were based on the STAR-CCM+ manual [17]. The skewness angle between cell faces should ideally remain below 85°, though values up to 90° are acceptable near boundaries as mentioned in the theory. The volume change value should preferably exceed 0.01, and the face validity is ideally 1.0.

Prism layers were used to resolve the high gradients close to the wall and sets different criteria of what y^+ should be for different turbulence models. For the realizable k-ε model the prism layer requires $y^+ < 5$ according to [28]. The prism layer total thickness was set to 3mm for all regions in the model.

A mesh independence study was conducted, where the original mesh was systematically coarsened for each of the three regions. Mesh independence was validated by analyzing pressure, momentum, and efficiency variations. Additional details regarding the different mesh settings can be found in Appendix A.1. The acceptable mesh criteria were defined such that the parameters remained within 1% of the original values, with continuity and momentum residuals below 10^{-4}. The values was set using a practical industrial standard according to [29].

After selecting a suitable mesh for the original case, the next step involved modifying the volume of the "box" surrounding the fan at the outlet. Following these geometric adjustments in the outlet region, the surface repair tool was used to refine the surface geometry elements. The surface cell size for the walls of the "box" was set to 5 mm, while a finer resolution of 1 mm was applied around the bars supporting the fan assembly where they intersected with the walls, as illustrated in Figure 3.8.

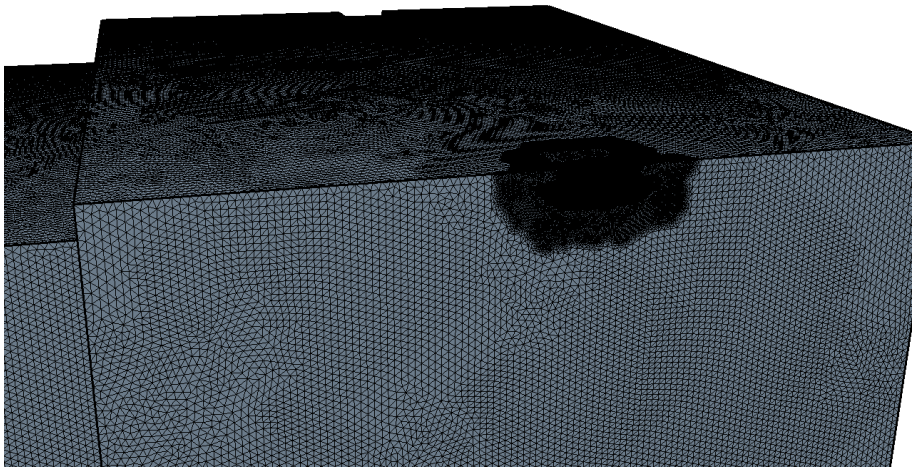

Figure 3.8: Visual of different cell sizes from surface meshing after surface repair.

3.4 Modification of Aspect Ratio

The aspect ratio refers to the relationship between the size of the fan and the size of its enclosure. In this study, the aspect ratio is specifically defined as the ratio between the characteristic length of the geometry and the radius of the fan. The characteristic length, in this context, refers to the distance from the surrounding enclosure walls to the center of the fan. To systematically analyze the effect of aspect ratio, only the height and width of the enclosure were modified, while the fan radius remained constant. This approach ensures a controlled investigation into how varying enclosure dimensions impact airflow behavior. This ratio is expressed using the following equation:

$$Aspect\ ratio = \frac{L}{\left(\frac{D_{fan}}{2}\right)} \tag{3.1}$$

The concept of aspect ratio is visually represented in Figure 3.9. The figure depicts a fan enclosed within a rectangular domain, where the height, width, and length define the enclosure's geometry. The modification of the aspect ratio is achieved by varying the height and width while maintaining a fixed fan size. This systematic adjustment allows for a detailed examination of how different configurations influence airflow dynamics, including velocity distributions, pressure variations, and turbulence intensity.

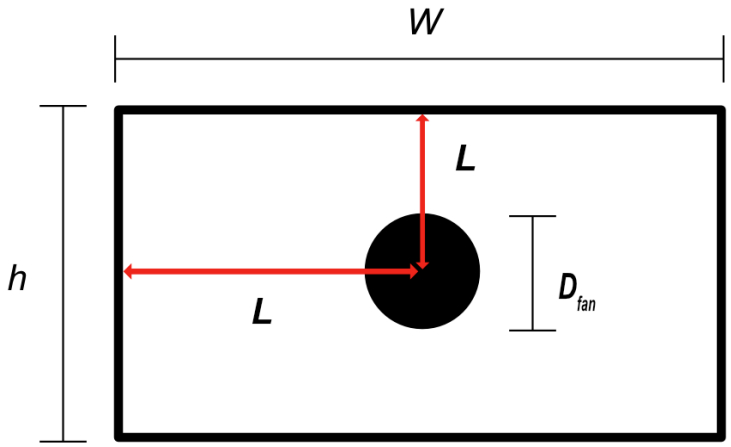

Figure 3.9: Aspect ratio

To assess the impact of aspect ratio on fan performance, a structured approach was employed. The study commenced with the smallest enclosure configuration, constrained by the outlet size. Incremental increases in both height and width were introduced while maintaining a constant fan radius. By progressively modifying these enclosure dimensions, the analysis aimed to capture the effects of different aspect ratios on airflow efficiency and pressure losses. The original case has the height-to-diameter and width-to-diameter ratios according to Table 3.4.

Table 3.4: Aspect ratio original case

Width Ratio\Height Ratio	1.287
2.433	Original Case

The testing began with Case A1, representing the smallest feasible enclosure size based on design constraints. From this baseline, the enclosure was progressively expanded by increasing both the height and width of the outlet box relative to the fan diameter. The full range of configurations is detailed in Table 3.5, where each case (e.g., A1, B2, D4) represents a specific combination of height-to-diameter and width-to-diameter ratios. The labels A through D correspond to increasing width ratios, while the numeric values 1 through 5 indicate increasing height ratios.

Table 3.5: Aspect ratio table

Width Ratio\Height Ratio	1.28	1.6	1.9	2.5	3
2.05	A1	A2	A3	A4	-
2.3	B1	B2	B3	B4	-
2.7	C1	C2	C3	C4	-
3.0	D1	D2	D3	D4	D5

In addition to the various cases presented in Table 3.5, based on the results from

the highest volume cases (C4,D4), Case D5 was selected for further analysis to assess whether the observed efficiency improvements continued or began to level off. The symmetric Case D5 characterized by height-to-diameter and width-to-diameter ratios of 3 and 3 was also examined to explore the effects of symmetric volume.

In addition to the modifications of height and width, the effect of varying the depth of the fan housing was also investigated. This was done to evaluate how changes in the axial wall distance influence the internal flow and overall fan performance. Due to project time constraints, the decision was made to limit this part of the study to a subset of configurations.

To investigate the effect of outlet depth while keeping the number of simulations manageable, three geometric configurations were selected: the original base case, Case C1, and Case C4. These two cases were chosen from Table 3.5 to represent contrasting enclosure sizes, C1 corresponding to a relatively compact geometry (low height and width relative to fan diameter), and C4 representing a significantly larger configuration. Their selection was motivated by the noticeable differences in flow behavior observed during the earlier aspect ratio simulations, making them particularly suitable for analyzing how outlet depth impacts fan performance.
For each of these three configurations, the depth of the outlet region was varied across four different values:

- the minimum feasible depth (based on geometric constraints),
- an intermediate depth between the minimum and the original value,
- the original depth from the baseline case,
- and a larger depth exceeding the original design.

To enable consistent comparison across configurations, the depth values were normalized using the ratio between the fan diameter and the axial outlet-wall distance. The corresponding ratios used in the simulations are summarized in Table 3.6.

Table 3.6: Depth ratio configurations

Configuration	**Minimum**	**Intermediate**	**Original**	**Large**
Depth Ratio	2.4	3.0	3.65	4.0

This enabled a targeted analysis of the impact of axial spacing on performance, complementing the previous results from height and width variations. The methodology remained consistent with the baseline simulations, using the same solver settings, meshing strategy, and boundary conditions to ensure fair comparison across cases.

3.5 Additional Elements

To further explore potential improvements in airflow performance and fan efficiency, this section investigates the influence of additional structural elements within the outlet region. Building upon the insights gained from the earlier simulations of the base configuration, the original geometry was used as a reference case for comparison.

The motivation for introducing these additional elements stemmed from the observations made in the efficiency and pressure distribution results. In particular, areas of flow separation, recirculation zones, and non-uniform velocity profiles near the outlet boundaries suggested the possibility of suboptimal flow behavior.

Each of the following modifications was implemented individually and in combination with others to isolate and evaluate their specific contributions to performance. The simulations were conducted using the same solver settings, mesh resolution, and boundary conditions as the base case to ensure comparability.

The impact of these additional elements was assessed primarily through changes in:

- Overall fan efficiency.
- Static pressure rise across the fan.
- Uniformity of the velocity profile at the outlet.
- Reduction in turbulent intensity and recirculation.

3.5.1 Cone Outlet Extension

A tapered extension was added to the outlet duct, gradually decreasing its cross-sectional area. The tapering was introduced to ease the flow expansion and reduce flow deceleration, thereby lowering pressure losses and turbulence intensity near the outlet.

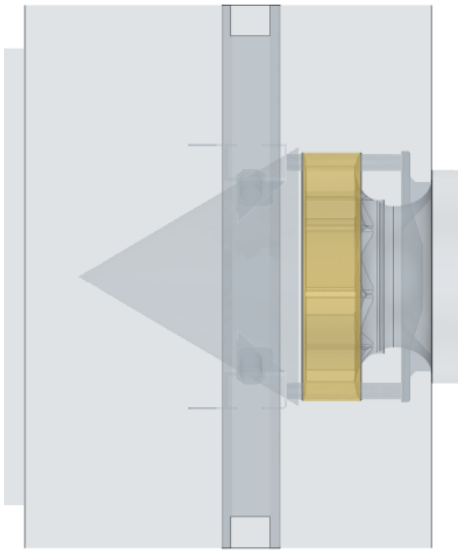

Figure 3.10: Cone

3.5.2 Cylinder Blockage

A cylindrical component was introduced in the gap between the fan assembly and the backplate, marked red in Figure3.11. The purpose of this modification was to investigate whether disrupting the low-pressure region typically observed in this area could enhance overall performance and efficiency.

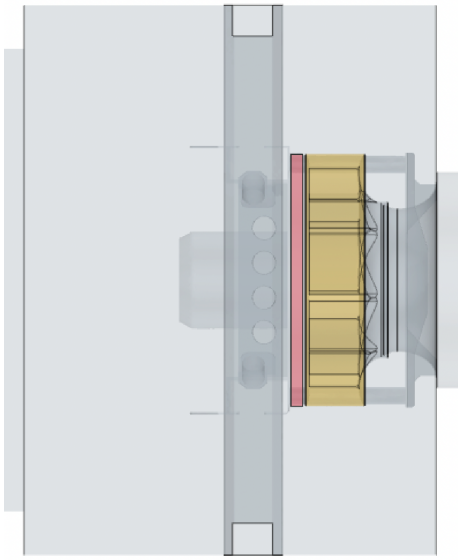

Figure 3.11: Cylinder

3.5.3 Rounded Corners

Sharp edges along the interior of the outlet enclosure were replaced with smooth rounded corners and straight rounded corners. This modification aimed to reduce boundary layer separation at the walls and promote smoother flow transitions, improving pressure recovery and reducing recirculation zones. Combing the previous elements with the two different rounded corners cases the following cases was tested.

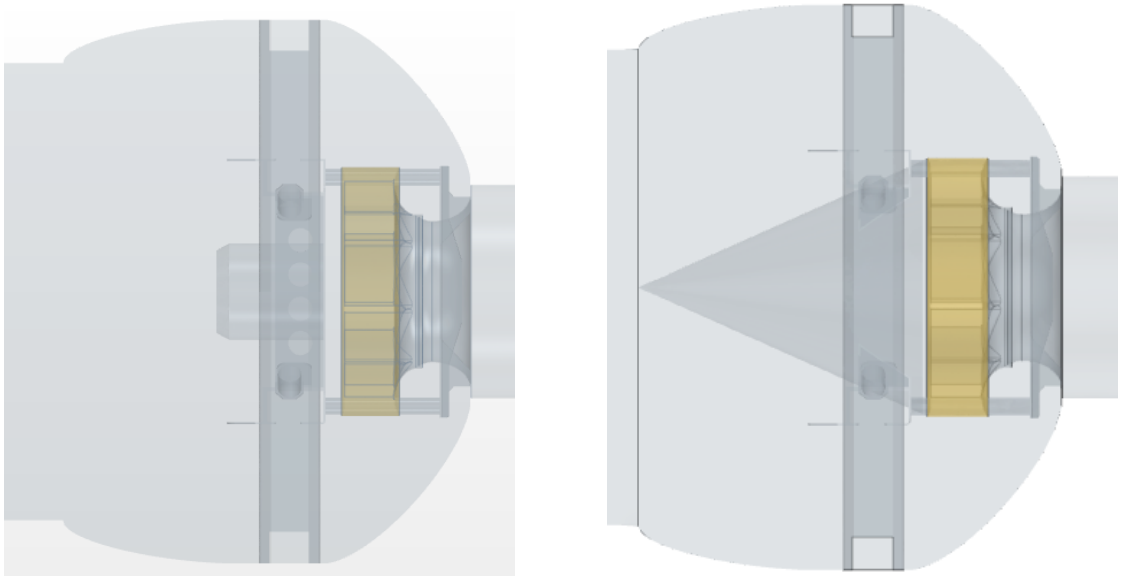

(a) Rounded corners (b) Rounded corners with cone

Figure 3.12: Comparison of rounded corners with and without cone

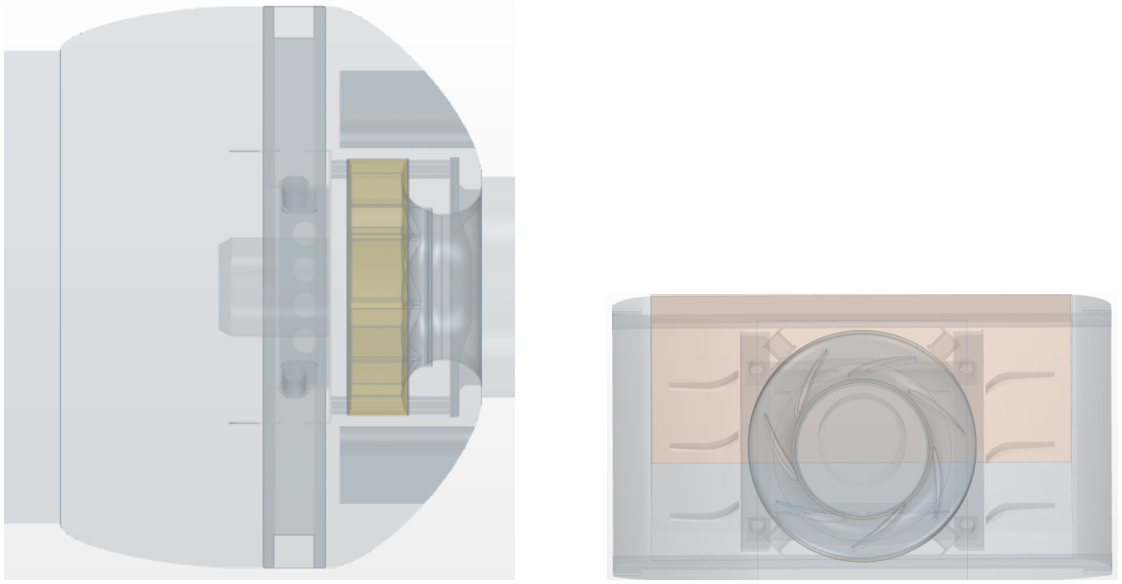

(a) Rounded corners with guide vanes (b) Guide vanes front view

Figure 3.13: Rounded corners with guide vanes from different views

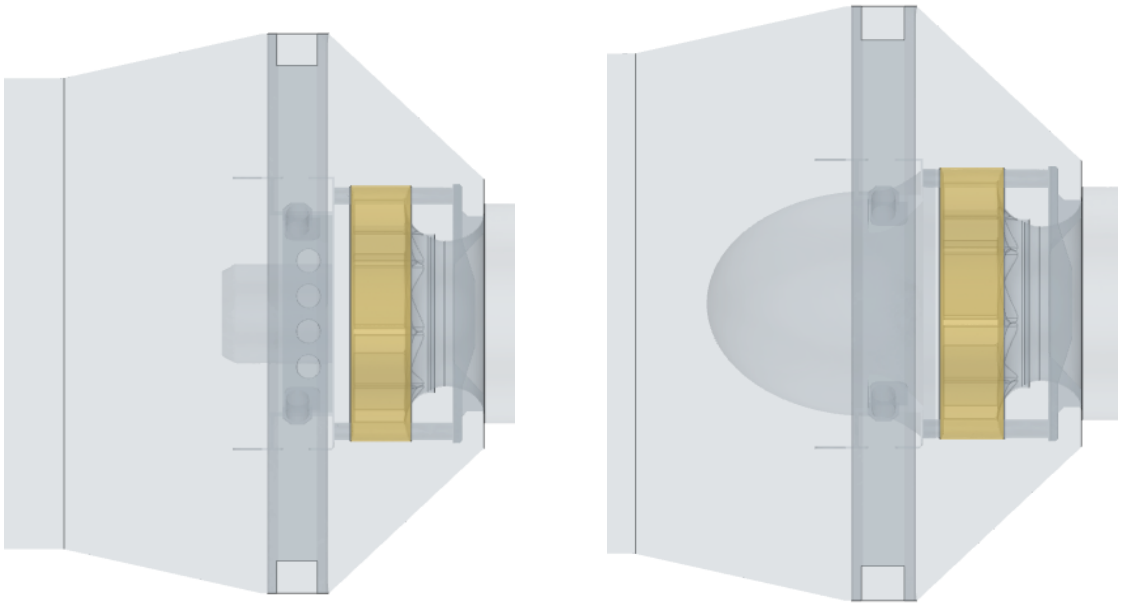

(a) Straight rounded corners (b) Straight rounded corners with cone

Figure 3.14: Straight rounded corners with and without cone

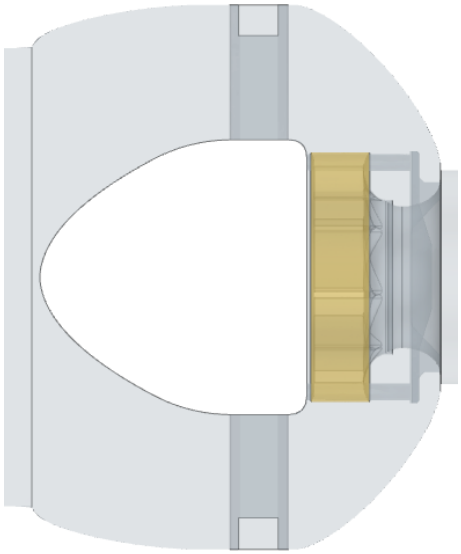

Figure 3.15: Rounded corners with wedge

4
Results

4.1 Mesh Independence Study

For the mesh independence study, we began with the original mesh provided by Swegon and systematically coarsened it in strategic steps. A total of eight different meshes were tested before identifying a mesh that exceeded the 1% deviation threshold compared to the original case. Table 4.1 presents the different mesh cases, the number of cells in each, and the percentage of cells relative to the original mesh. For a more detailed comparison of each mesh variation, Appendix A presents the original mesh parameters along with the size adjustments applied in each case.

Table 4.1: Mesh cases and cell count comparison

	Original	Case 1	Case 2	Case 3	Case 4	Case 5	Case 6	Case 7	Case 8
Cells (millions)	17.06	15.61	12.59	10.48	7.02	5.87	4.74	3.79	1.99
Percentage (%)	100	91.55	73.83	61.45	41.15	34.41	27.81	22.20	11.67

Figures 4.1, 4.2, and 4.3 illustrate the variations in pressure, fan torque, and efficiency across the different mesh cases. Additionally, Figure 4.4 shows the percentage deviation from the original mesh. The results indicate that the final mesh, Case 8, is too coarse, as the results fall outside the predefined limits.

Both Case 6 and Case 7 were selected for further simulations to evaluate the ratio of height to width. However, it was observed that as the geometry increased in size, the deviations became significant. Consequently, mesh Case 6 was chosen for continued simulations after simulating some of the height-to-diameter and width-to-diameter ratios cases and seeing that the results started to diverge for Case 7 compared to Case 6.

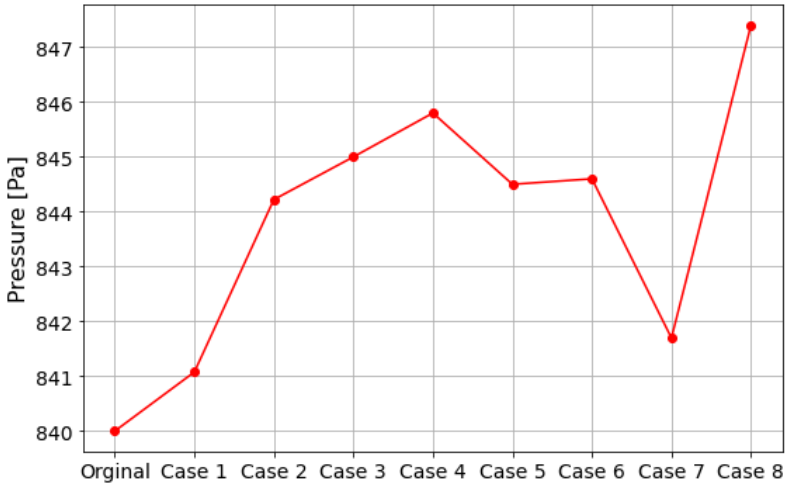

Figure 4.1: Pressure variation across cases

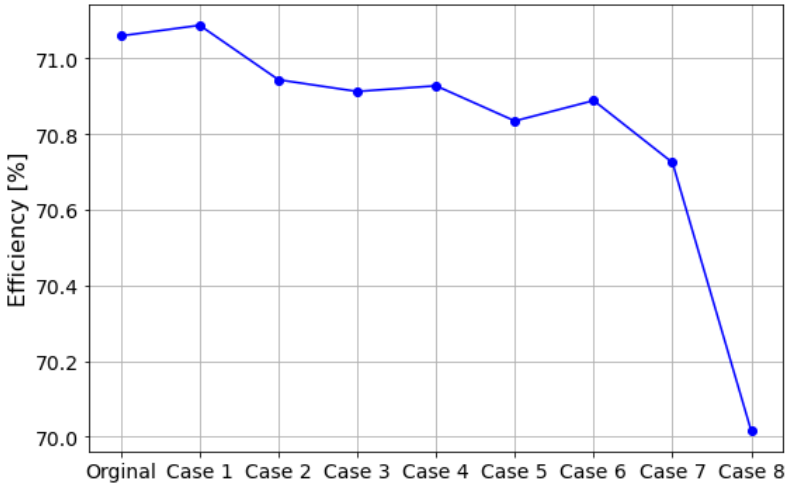

Figure 4.2: Efficiency variation across cases

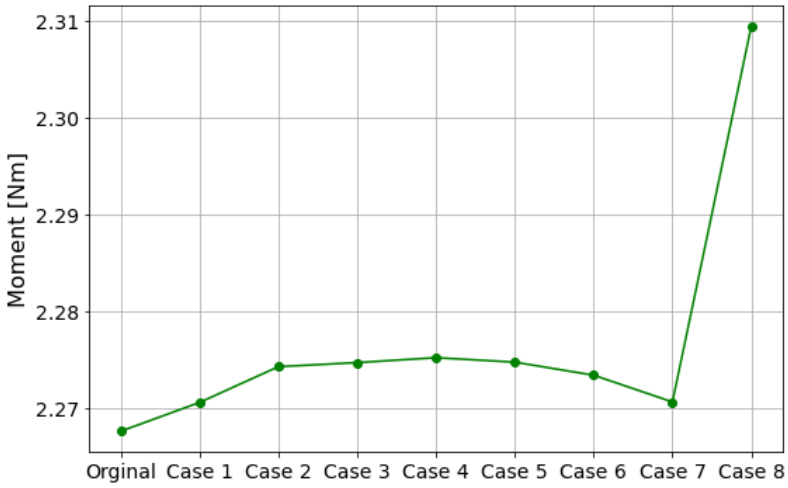

Figure 4.3: Moment variation across cases

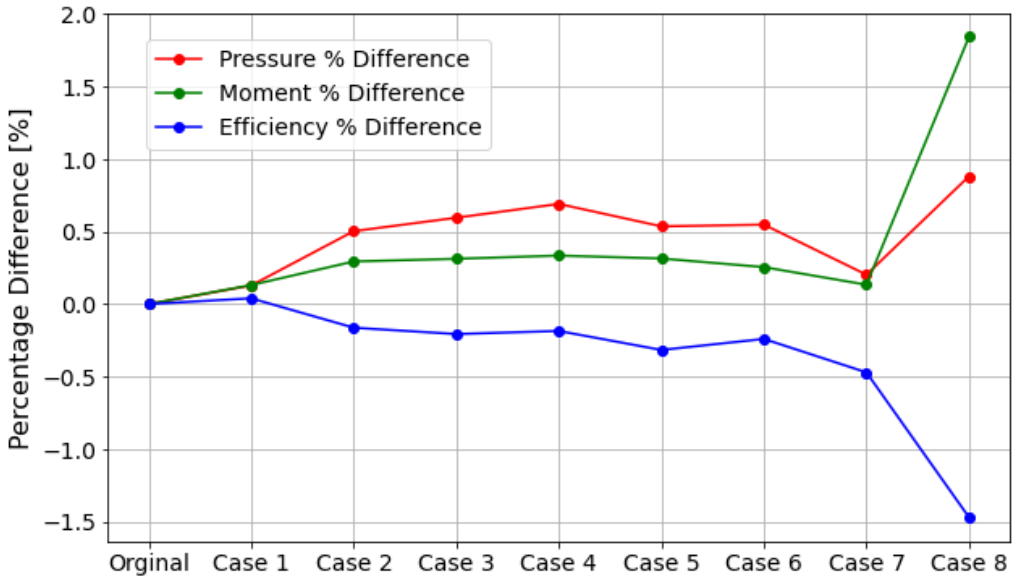

Figure 4.4: Percentage differences across cases

4.2 Fan Efficiency

The fan efficiency results presented in this section are based on a series of simulations where the height and width of the outlet enclosure were varied systematically. The goal was to evaluate how the aspect ratio between the wall distance and the fan diameter influences the performance of the system.

The simulations revealed a clear trend: as both the height and width of the outlet region increased, the fan efficiency improved. The initial increases in these dimensions resulted in a relatively steep rise in efficiency, which indicates that very compact designs impose significant aerodynamic penalties due to disturbed airflow patterns, recirculation, and high-pressure losses near the outlet walls. However, beyond a certain enclosure size, the rate of efficiency improvement diminished, suggesting an asymptotic behavior as the system approached an optimal geometric configuration.

Interestingly, the analysis also revealed a non-linear relationship between the height and width adjustments. While increasing both dimensions simultaneously led to consistent gains in efficiency, modifying only one, particularly the width, while keeping the other fixed at a lower value, sometimes resulted in a reduction in overall performance. This was most evident in the cases where the height remained low but the width was significantly extended. In such configurations, asymmetric flow development and increased lateral turbulence appeared to negatively impact the pressure recovery and flow uniformity.

Figure 4.5 illustrates the interpolated surface of fan efficiency as a function of the ratio between outlet height and width relative to the fan diameter. A clear efficiency plateau can be seen toward the higher end of the tested ratios, which supports the

idea that beyond a certain spatial allowance, further increases in enclosure size yield diminishing returns. This trend is evident in Case D5, where the efficiency did not improve beyond the levels observed in Cases C4 and D4. Table 4.2 provides the raw efficiency values used to generate the figure.

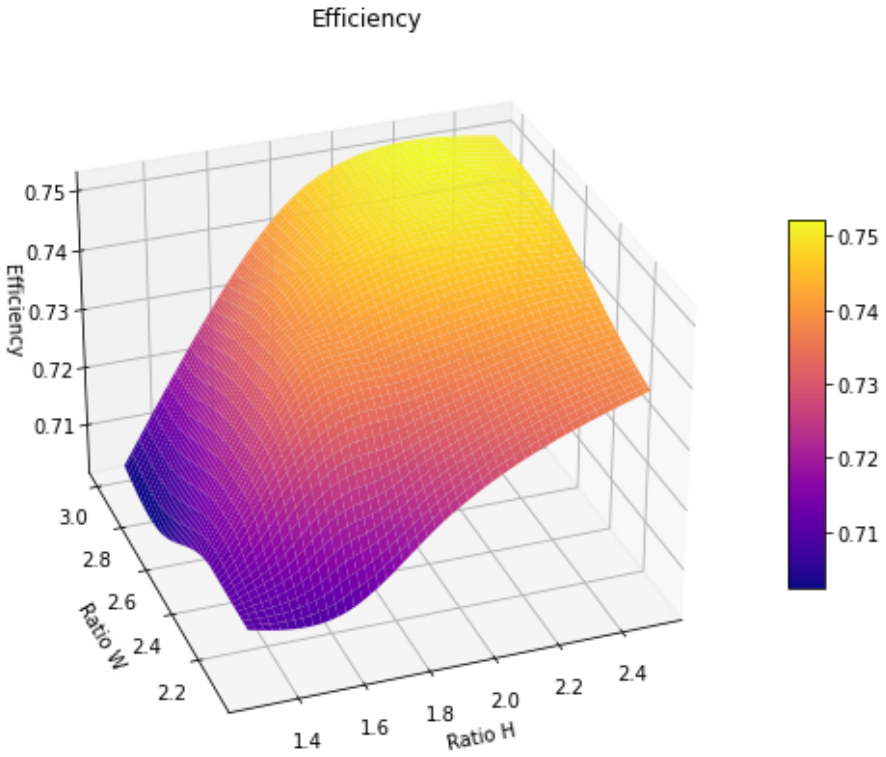

Figure 4.5: Efficiency as a function of Ratio H and Ratio W.

Table 4.2: Table showing efficiency values for different Height/Width and corresponding ratios

Width Ratio/Height Ratio	1.2799	1.6	1.9	2.5	3
2.0478	71.1	71.2	72.4	73.8	-
2.3	71.2	73.3	73.6	74.4	-
2.7	70.3	73.6	74.8	75.0	-
3	70.4	73.1	74.8	75.0	75.0

4.3 Pressure Rise

While fan efficiency provides a holistic measure of energy conversion within the system, evaluating the static pressure rise across the fan offers critical insight into the aerodynamic behavior of the airflow. This section presents the pressure rise results obtained from simulations of various outlet-wall configurations and examines how

the enclosure geometry influences the pressure buildup within the AHU.

The pressure rise in this study is defined as the difference in static pressure between the inlet boundary of the inlet region and the outlet boundary of the outlet region.

The simulations demonstrate a strong correlation between pressure rise and the geometric dimensions of the outlet enclosure. As both the height and width of the outlet region increased relative to the fan diameter, the pressure rise improved consistently across nearly all configurations. This trend aligns well with the efficiency results discussed in Section 4.2 and is indicative of improved flow recovery and reduced aerodynamic losses.

Table 4.3 presents the pressure rise values for a range of height-to-diameter and width-to-diameter ratios. These values were used to generate the interpolated surface shown in Figure 4.6, except Case D5. The figure reveals that configurations with both increased height and width exhibit the greatest pressure rise, while more compact configurations tend to restrict flow expansion and increase local turbulence, thereby reducing the effective pressure buildup.
Moreover, an important observation is that increasing only one geometric parameter, particularly the width, while keeping the other relatively small, did not yield significant gains in pressure rise. In some cases, the pressure rise actually decreased compared to the baseline. This suggests that imbalanced outlet geometries can lead to uneven flow development and asymmetric pressure fields, which may contribute to localized separation or swirling behavior downstream of the fan.

The observed results highlight that pressure rise, much like fan efficiency, benefits from a balanced and moderately expanded enclosure geometry. However, after a certain threshold, particularly when height and width exceed approximately 2.5 to 3 times the fan radius, further increases in size result in diminishing returns. This plateau suggests that most of the recoverable pressure has already been obtained, and the system reaches an optimized aerodynamic state.

In summary, the pressure rise analysis reinforces the findings from the efficiency study and provides a complementary perspective on the importance of outlet-wall spacing. Optimizing both the height and width of the outlet enclosure simultaneously is critical for maximizing pressure recovery and ensuring stable, efficient operation of the fan within the AHU.

Table 4.3: Table showing second dataset values for different Height/Width and corresponding ratios

Width Ratio/Height Ratio	1.2799	1.6	1.9	2.5	3
2.0478	842	842	856	873	-
2.3	846	861	866	878	-
2.7	838	868	881	885	-
3	838	865	880	884	885

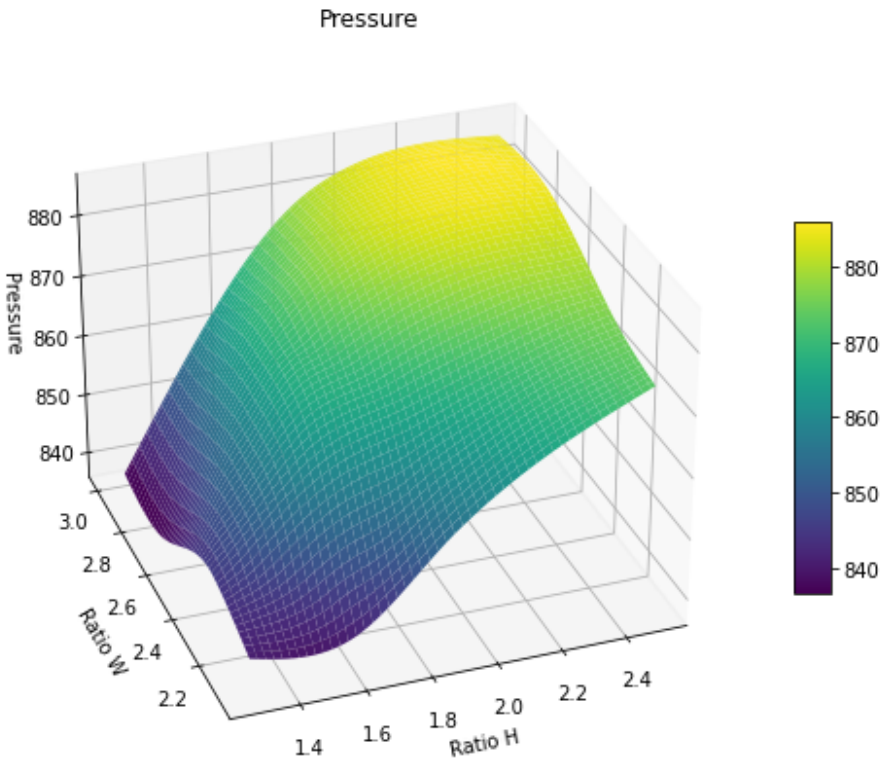

Figure 4.6: Pressure as a function of Ratio H and Ratio W.

4.4 Varying Depths

Next, the effect of outlet depth was investigated by examining three configurations: the original case, Case C1, and Case C4, as listed in Table 4.2. Among the C-series cases, C1 exhibited the lowest fan efficiency, while C4 showed one of the highest. These two cases were selected to represent opposite ends of the performance spectrum and were compared to the original case to evaluate how variations in outlet depth influence fan behavior.

As shown in Figure 4.7, increasing the depth beyond that of the original case (corresponding to a length ratio of 3.65) resulted in only a minor improvement in efficiency, even at a length ratio of 4.0.

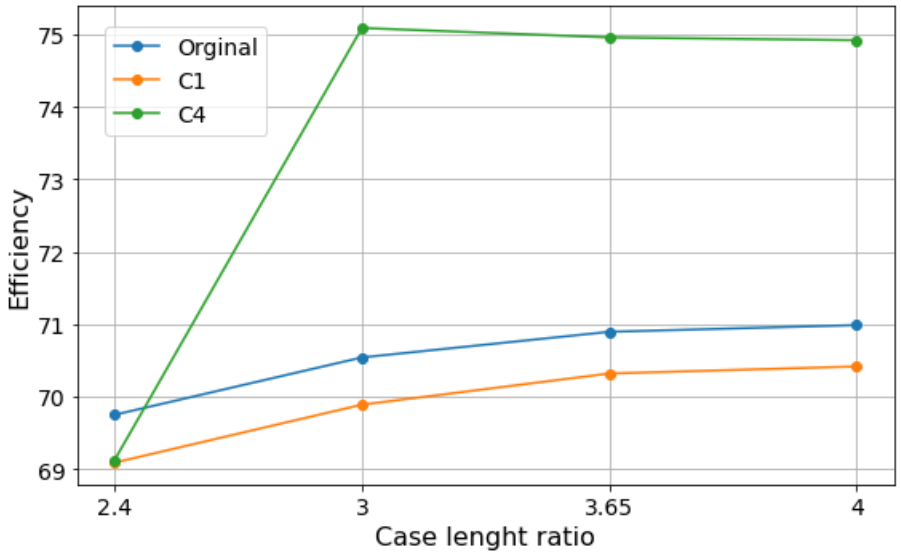

Figure 4.7: Efficiency for different depth ratios for different cases

Table 4.4: Table showing different efficiency values for different length ratios

Depth Ratio	2.4	3.0	3.65	4.0
Original case	69.7	70.6	70.9	71.0
C1	69.1	69.9	70.3	70.4
C4	69.1	75.1	75.0	74.9

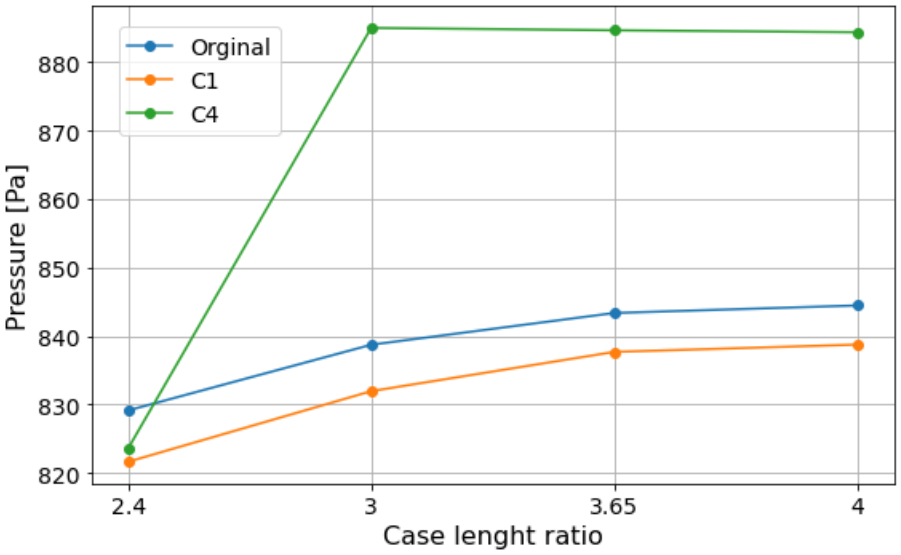

Figure 4.8: Pressure for different depth ratios for different cases

Table 4.5: Table showing different pressure values for different length ratios

Depth Ratio	2.4	3.0	3.65	4.0
Original	829	839	843	844
C1	822	832	838	839
C4	824	885	885	884

Case C4 exhibited a noticeable jump in both pressure rise and efficiency when increasing the length ratio from 2.4 to 3.0. This sharp improvement contrasts with the more gradual trend observed in the smaller volume configurations, where efficiency gains diminished progressively with increased length. In Case C4, the improvement appears to level off quickly, suggesting a different flow response and indicating that the optimal depth may have been reached earlier. For detailed numerical values, refer to Table 4.5.

Comparing the static pressure distribution in Figure 4.9 for Case C4, with a depth ratio of 2.4, to the original case shown in Figure 4.11(d), a significant change in static pressure is observed. Similarly, the velocity fields presented in Figures 4.10 and 4.13(d) exhibit notable differences. These results indicate that the altered geometry restricts the flow, thereby reducing the overall efficiency of the system.

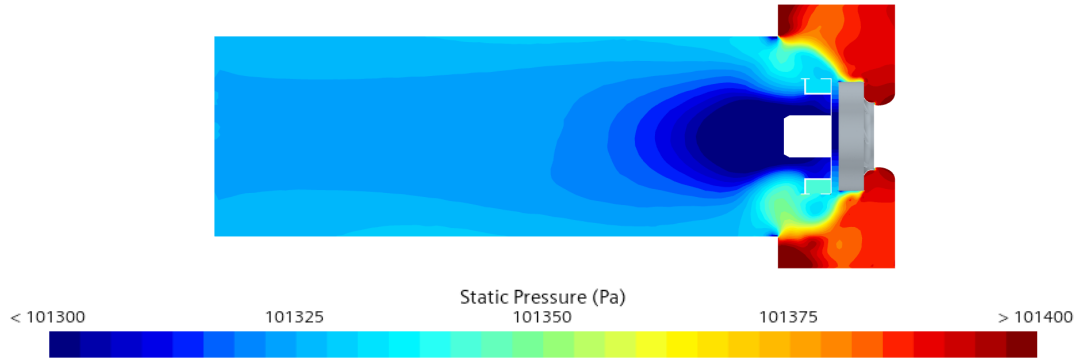

Figure 4.9: Static pressure distribution - Case C4, depth ratio 2.4

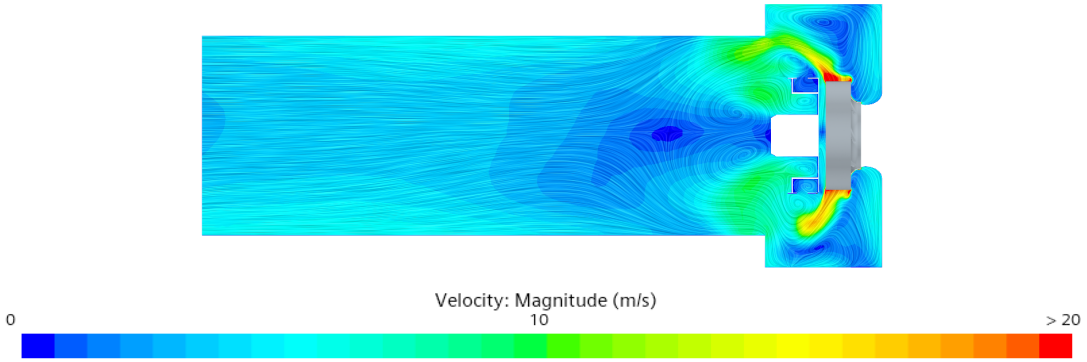

Figure 4.10: Velocity magnitude – Case C4, depth ratio 2.4

4.5 Scalar and Vector Plots

To further understand the internal flow structures and their influence on fan performance, scalar and vector field visualizations were generated. These included static pressure, velocity magnitude, and turbulent kinetic energy distributions for different enclosure configurations (Cases C1–C4). The plots provide valuable insight into the aerodynamic behavior under varying outlet-wall distance conditions.

4.5.1 Static Pressure

Figures 4.9 and 4.10 illustrate the static pressure distribution in the z- and x-view planes across the four configurations. As the enclosure volume increases from Case C1 to C4, a more uniform pressure field develops. Notably, low-pressure regions near the fan outlet become less pronounced, indicating improved flow recovery. The more compact Case C1 exhibits greater pressure gradients, which can contribute to reduced efficiency due to localized losses and backpressure effects.

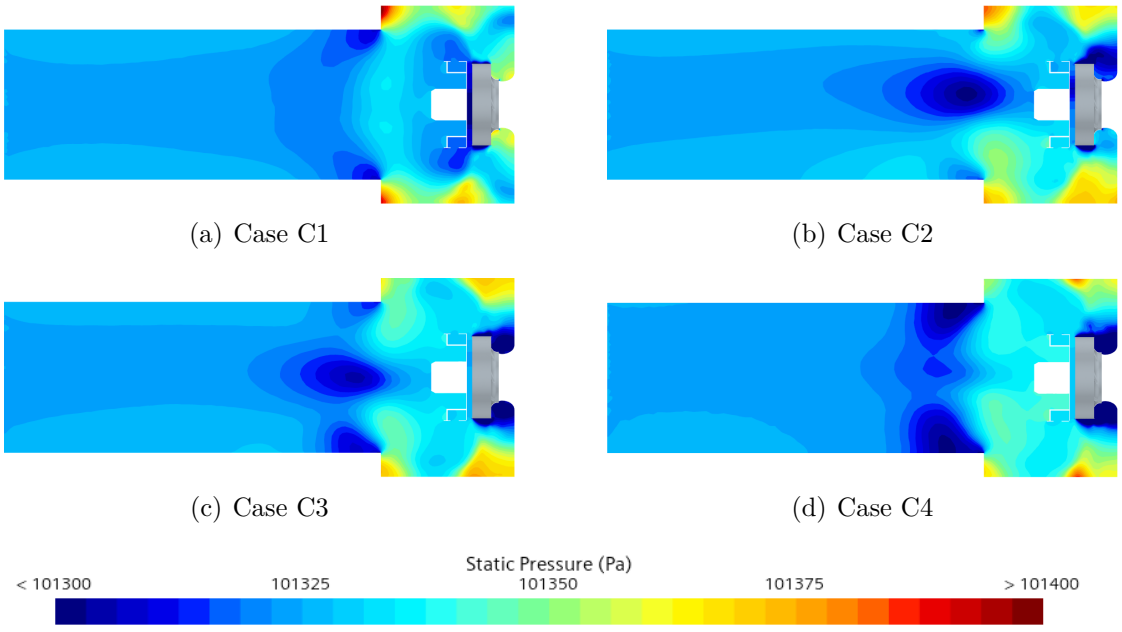

(a) Case C1 (b) Case C2

(c) Case C3 (d) Case C4

Figure 4.11: Static pressure distribution across four cases in z-view.

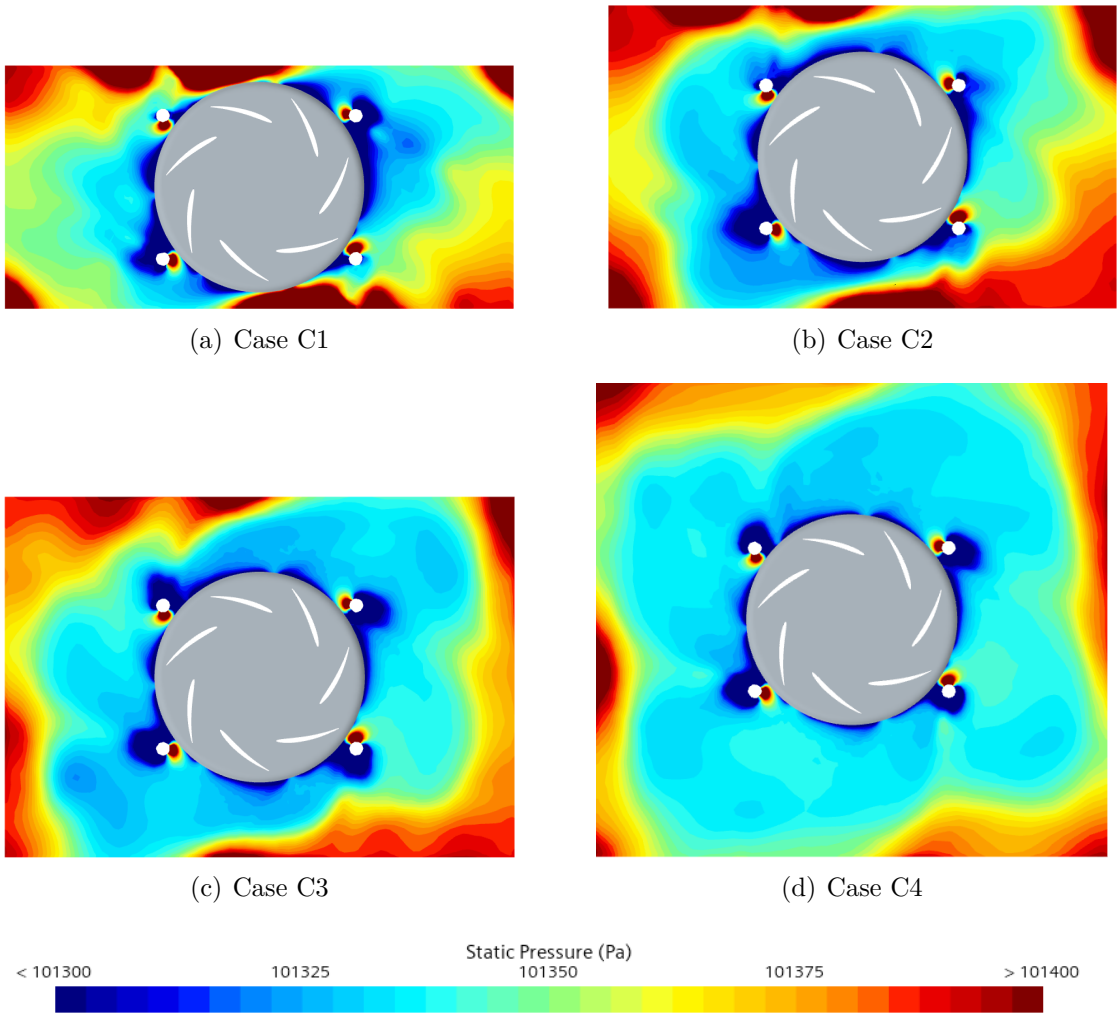

(a) Case C1

(b) Case C2

(c) Case C3

(d) Case C4

Figure 4.12: Static pressure distribution across four cases in x-view.

4.5.2 Velocity Magnitude

Figures 4.11 to 4.12 display the velocity magnitude fields for each case. A clear trend emerges where flow uniformity and outlet directionality improve with increased outlet enclosure size. In Case C1, the flow appears more scattered with significant recirculation zones, particularly around the outlet periphery. By Case C4, the velocity field becomes more streamlined and focused along the outlet duct axis, reflecting reduced turbulence and more effective momentum transfer

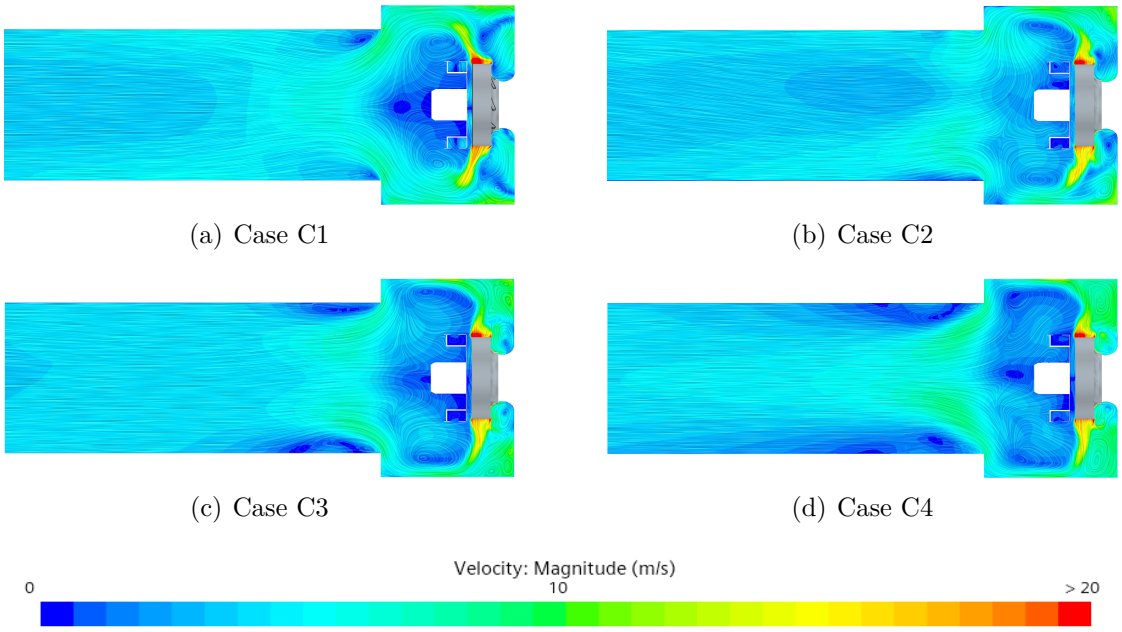

(a) Case C1 (b) Case C2

(c) Case C3 (d) Case C4

Figure 4.13: Velocity magnitude distribution across four cases in z-view.

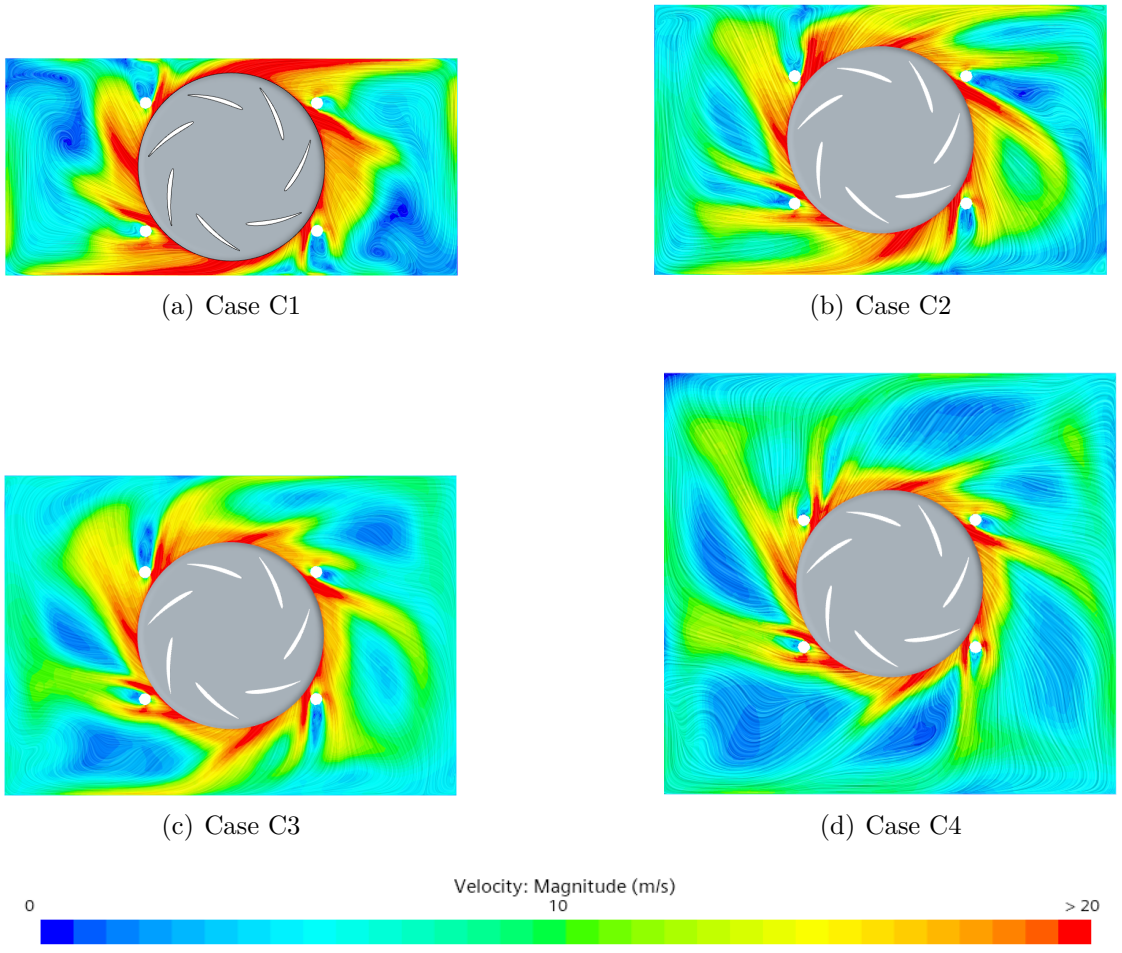

(a) Case C1 (b) Case C2

(c) Case C3 (d) Case C4

Figure 4.14: Velocity magnitude distribution across four cases in x-view.

4.5.3 Turbulent Kinetic Energy

The turbulent kinetic energy (TKE) plots reveal the distribution of turbulence intensity across the domain. As seen in Figure 4.13 and 4.14, smaller enclosures like C1 exhibit elevated turbulence levels near walls and at the outlet, associated with confined and chaotic flow patterns. In contrast, Case C4 demonstrates lower TKE concentrations and smoother gradients, supporting the observed improvements in both fan efficiency and pressure recovery.

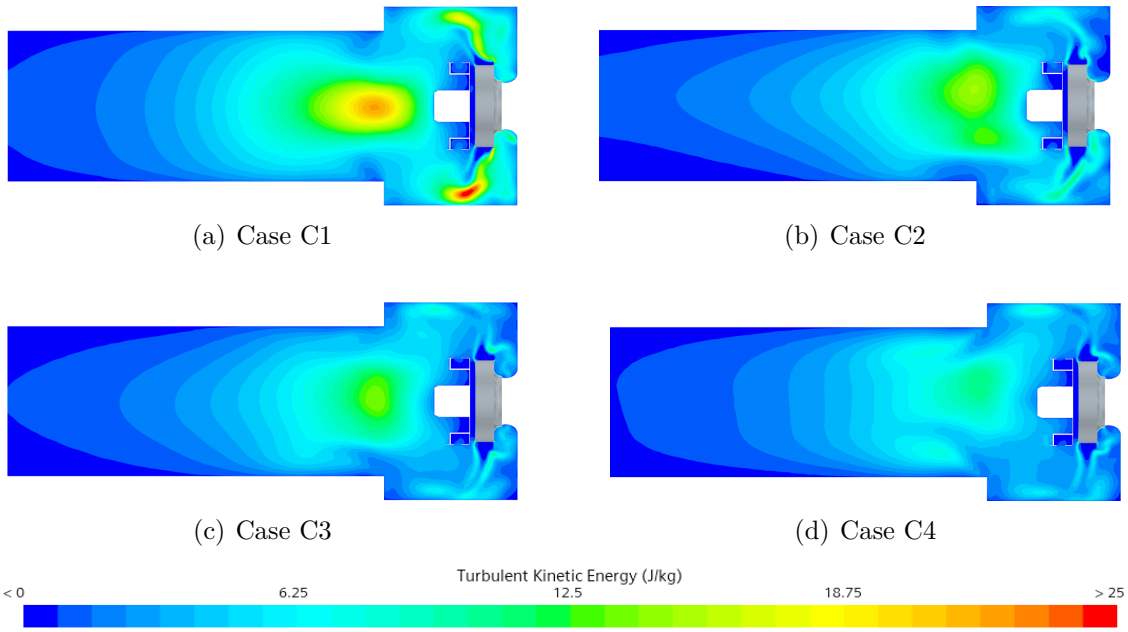

(a) Case C1 (b) Case C2

(c) Case C3 (d) Case C4

Figure 4.15: Turbulent kinetic energy across four cases in z-view.

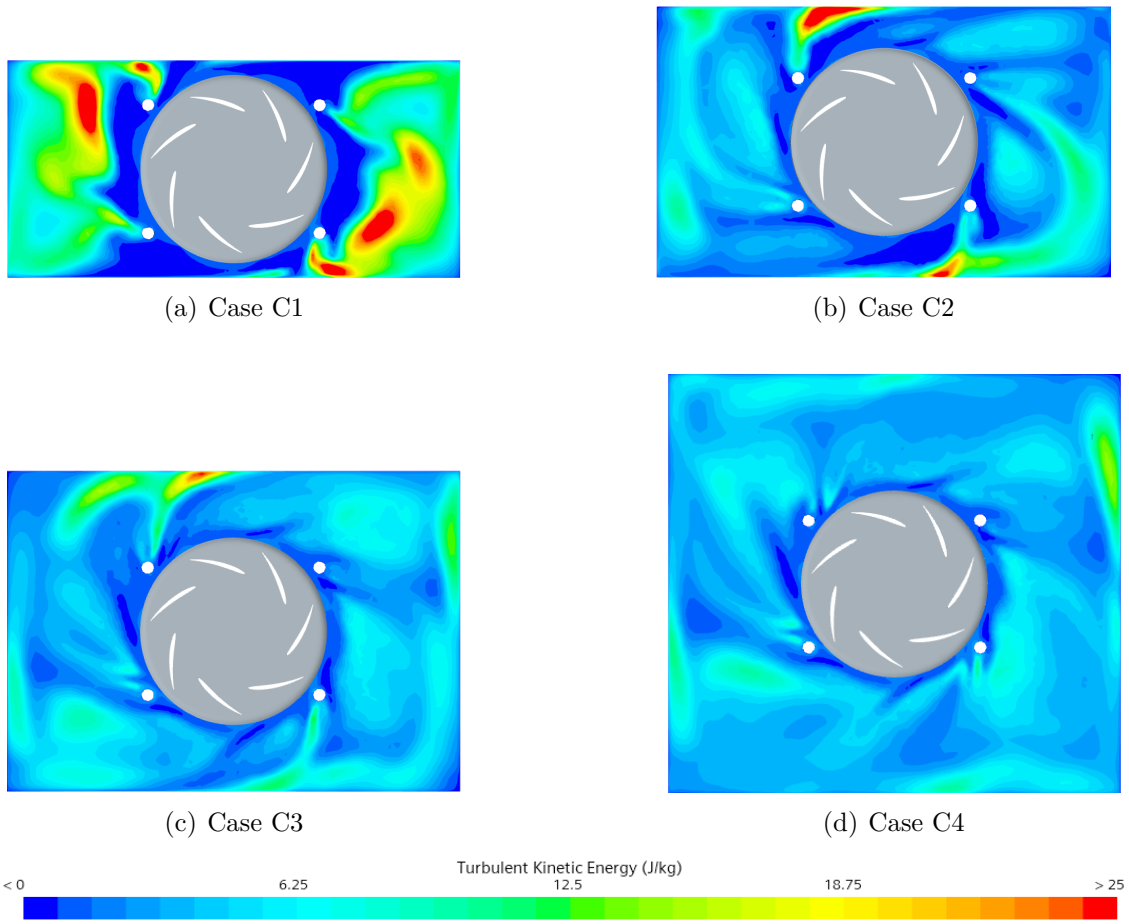

(a) Case C1

(b) Case C2

(c) Case C3

(d) Case C4

Figure 4.16: Turbulent kinetic energy across four cases in x-view.

4.6 Additional Elements

After simulating the original case, we analyzed the pressure distribution and other flow properties within the volume. This analysis informed the development of simple geometric modifications that could feasibly be implemented within the AHU.

Figures for Case C1 above can be used as a visual reference, as this configuration closely resembles the original case in both geometry and flow characteristics. While not used as a basis for the design process, these figures help illustrate the type of flow features observed in the original case. Observations from the results formed the basis for implementing geometric modifications aimed at enhancing the flow and increasing the efficiency. One of the key observations was the presence of a low pressure zone behind the fan assembly. To address this, a cone was introduced, additionally a cylindrical insert was tested to mitigate another low pressure zone in the same area. Both modifications led to a significant improvement in flow efficiency.

Next, we investigated the effect of smoothing the volumes corners to help guide airflow more effectively toward the outlet duct. The rounded corner configuration

improved flow guidance but also introduced a large backflow into the gap near the fan, which disrupted the flow more than in the straight cornered configuration. Despite this, the performance of rounding the corners was comparable to that of the cone and cylinder individually.

Subsequently, we combined the geometric elements cone, cylinder, and rounded corners which resulted in a marked increase in overall efficiency. The corresponding improvements relative to the original case are depicted in Figure 4.17, while the efficiency values for the various configurations are shown in Figure 4.18.

Following the previous modifications, guide vanes and a large wedge were introduced to further investigate potential improvements in flow behavior. The guide vanes, however, did not yield a noticeable enhancement in airflow. This limited impact is attributed to the fact that they were not designed to the specific flow conditions, they were implemented as a conceptual test. Due to time constraints, no further optimization of the guide vane design was looked into.

Additionally, a wedge spanning from the top to the bottom of the volume was implemented in combination with the rounded corner configuration. While the intention was to further direct the airflow, this setup instead restricted the flow path and led to a reduction in system pressure, as shown in Figure 4.19. The resulting pressure drop negatively affected the overall efficiency.

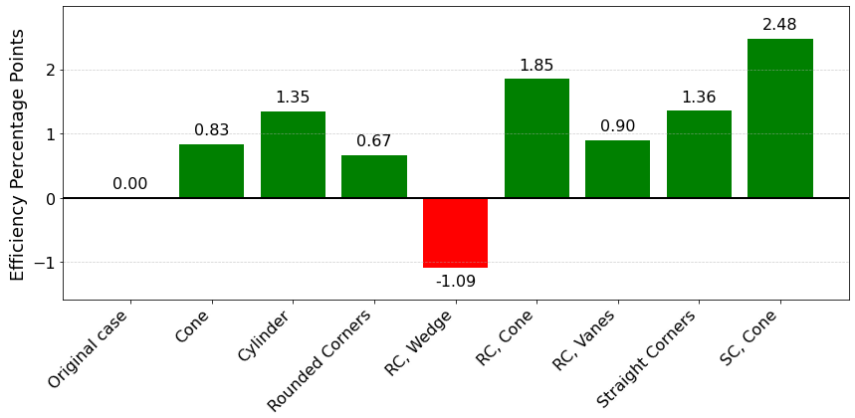

Figure 4.17: Efficiency percentage points difference

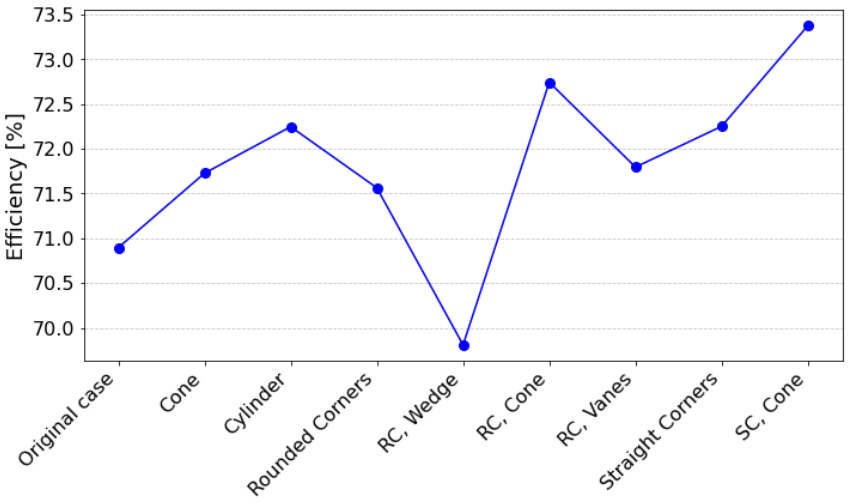

Figure 4.18: Efficiency across element cases

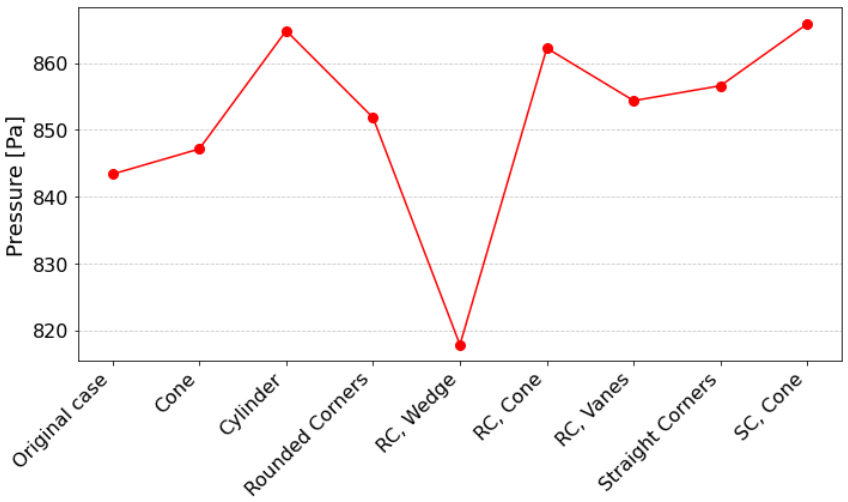

Figure 4.19: Pressure Across Element Cases

5

Discussion

5.1 Interpretation of Results

The simulations performed in this study reveal a clear relationship between outlet-wall spacing and fan performance. Increasing the height and width of the enclosure surrounding the plenum fan significantly reduced recirculation zones and turbulence intensity, resulting in smoother flow development and increased efficiency. These improvements manifested in increased fan efficiency and higher static pressure rise across the fan. The results showed that highly compact enclosures impose significant aerodynamic penalties. In tight geometries, flow leaving the fan interacts more strongly with nearby walls, causing non-uniform velocity fields, increased swirl, and localized pressure drops. These effects ultimately reduce the effective work done on the air, thereby lowering efficiency.

Notably, a point of diminishing returns was observed. As the outlet enclosure dimensions grew beyond a certain threshold, around 2.5 to 3 times the fan radius, performance gains began to plateau. This indicates the presence of a geometric "sweet spot" where performance is optimized without unnecessary increases in system volume. Oversizing the enclosure beyond this point offers little to no performance benefits and may introduce practical disadvantages such as material use, cost, and footprint.

5.2 Influence of Geometric Modifications

Beyond the primary aspect ratio study, the investigation of geometric enhancements provided further insights. The addition of a conical extension at the outlet helped guide flow more smoothly into the duct, reducing abrupt expansion and related pressure losses. The cylindrical blockage near the fan outlet effectively minimized recirculation zones in its vicinity by redirecting central flow.

Rounded corners at the edges of the outlet region were also tested to and made a big impact helping the flow move out of the volume. These modifications were found to reduce separation at sharp edges, which in turn improved pressure recovery. Interestingly, combining the cone, cylinder, and rounded corners into a single configuration yielded the highest observed efficiency gains, highlighting the synergistic effect of multiple flow-smoothing elements.

These results demonstrate that relatively simple physical modifications can significantly influence the flow field and should be considered in early-stage design processes for compact AHUs.

Due to the scope of this report and time constraints, different element implementations were not investigated in advance. Only after completing all simulations and implementing the elements did we discover that Swegon holds a patent [30] for a cone design around the fan assembly, intended to reduce backflow into the low-pressure region and increase the efficiency of the system.

5.3 Mesh Quality and Limitations

Despite efforts to ensure mesh independence, the mesh resolution remains a potential source of uncertainty in the results. Although all final meshes used prism layers and polyhedral cells to balance quality and computational cost, the high-gradient regions near the fan blades, wall boundaries, and separation zones may not have been resolved finely enough to capture all the relevant flow physics accurately.

The skewness angle, cell quality, and residuals were monitored and kept within acceptable ranges according to STAR-CCM+ guidelines. However, this does not guarantee that the solution is entirely mesh independent. It is possible that pressure gradients and turbulence metrics, especially near solid boundaries and interfaces, are under resolved in some configurations. This could slightly alter quantitative results such as static pressure rise and turbulent kinetic energy distributions.

Future work should consider applying local mesh refinement strategies, especially in regions with sharp curvatures or high velocity gradients, and assess result sensitivity to these refinements. While the current mesh provides a reliable basis for comparing trends between cases, its resolution is likely insufficient for high fidelity turbulence or acoustic studies.

5.4 Use of Interpolation and Surface Mapping

To better visualize the relationship between geometric parameters and performance metrics, interpolated surface plots were used. These surfaces were constructed from discrete simulation results for varying height-, width- and depth-to-diameter ratios. Interpolation helped reveal continuous trends in the data and identify regions where efficiency gains began to level off.

While this visualization approach is useful for understanding general behavior and informing design decisions, it comes with inherent limitations. The accuracy of interpolated surfaces depends heavily on the resolution and distribution of data points. In this study, the number of simulated cases was limited by time and computational resources, particularly for combinations involving depth variations and modified geometries.

As a result, the interpolated surfaces may smooth over local variations and potentially under represent nonlinear interactions between geometric parameters. For instance, sharp performance changes that could occur due to flow instabilities or resonance effects might be missed if they fall between sampled points. Therefore, while interpolation offers valuable design insights, the results should not be interpreted as exact predictions but rather as indicative trends. Engineers and designers should use these visualizations to guide further targeted simulations or physical tests, particularly in regions where small changes in geometry lead to relatively large changes in performance.

5.5 Model and Methodology Constraints

The study employed a steady-state approach using the Moving Reference Frame technique, which is suitable for modeling rotating machinery under quasi-steady conditions. While this method is computationally efficient and captures the time-averaged effects of rotation, it does not resolve transient behaviors such as vortex shedding, pulsating wake structures, or periodic blade-passing effects. However, due to time constraints, the steady-state simulations are considered sufficient for this project. Approximately 40 simulations have been conducted, each requiring 1–2 days to reach convergence.

These dynamic features, though not critical for assessing general trends in efficiency, can have a significant influence on acoustic performance, fan longevity, and detailed pressure fields. Capturing such phenomena would require unsteady simulations using techniques like the sliding mesh method or Large Eddy Simulation (LES). These models provide richer flow information but at a significantly higher computational cost and model complexity.

Additionally, all walls were modeled as smooth and adiabatic. In real systems, surface roughness and thermal gradients may influence boundary layer behavior and flow stability. Such factors were not considered in this study and may slightly shift actual performance in experimental settings.

5.6 Practical Implications

From a practical standpoint, this study provides actionable insights for the HVAC industry and specifically for manufacturers like Swegon. It confirms that modest increases in outlet-wall spacing can significantly improve fan performance, but also highlights that there is an upper limit beyond which additional volume provides little benefit. For compact AHU systems, integrating geometric enhancements such as cones, rounded corners can achieve better performance without increasing enclosure size.

The results support a design philosophy that favors targeted, efficient spatial allocation rather than indiscriminate scaling. Moreover, the interpolation approach enables engineers to quickly assess trade offs between space and performance in early design stages.

While the findings are most directly applicable to the specific fan and setup studied, the physical principles and performance behaviors observed are transferable to a wide range of ventilation system designs.

6
Conclusion

This study investigated how the outlet wall distance affects fan efficiency in an Air Handling Unit (AHU), using steady-state Computational Fluid Dynamics (CFD) simulations. The primary focus was to analyze how variations in the aspect ratio between the fan diameter to the height, width, and depth of the outlet enclosure, impact airflow behavior, pressure recovery, and overall fan performance.

The simulations demonstrated a clear correlation between increased enclosure size and improved fan efficiency. Compact configurations led to disturbed flow structures, elevated turbulence, and recirculation zones near the outlet, all of which contributed to aerodynamic losses. As the enclosure dimensions were increased, these effects diminished, resulting in improved flow uniformity, lower turbulence intensity, and higher static pressure rise.

However, the results also revealed diminishing returns beyond certain threshold values of height, width, and depth. Once the spatial constraints exceeded approximately 2.5 to 3 times the fan radius, further increases in enclosure size had minimal impact on performance. This suggests the existence of an optimal enclosure configuration, beyond which additional volume offers limited aerodynamic benefit.

The study also explored simple geometric enhancements such as cone outlet extensions, cylindrical blockages, and rounded corners. These modifications showed a measurable improvement in flow performance. In particular, combining all three elements resulted in the highest gains in efficiency and pressure recovery, offering practical design strategies for compact AHUs.

Although the results are based on numerical simulations, they offer valuable design insights for optimizing outlet geometries in plenum fan configurations. Future work should include transient simulations using sliding mesh techniques and experimental validation of key configurations to further substantiate the findings.

Overall, the findings from this thesis provide a solid foundation for improving the aerodynamic performance and energy efficiency of modern HVAC systems, particularly in applications where space constraints challenge optimal airflow design.

7
Future Work

To build on the findings of this study, the following areas are recommended for future exploration:

- Conduct physical experiments to validate the CFD results and quantify any deviations.
- Perform transient simulations to capture unsteady phenomena in the flow field.
- User a finer mesh for the element cases.
- Investigate the impact of fan operating RPM, inlet conditions.
- Investigate the effects of using a larger fan.
- Examine noise and vibration characteristics of different aspect ratio configurations.

Bibliography

[1] Magnus Ekh. *Introduction to Continuum Mechanics*. Accessed: Feb. 14, 2025. Göteborg, Sweden, 2020. URL: https://www.tfd.chalmers.se/~lada/MoF/postscript/lecture_notes_continuum_mechanics_2020.pdf.

[2] Lars Davidson. *Fluid Mechanics, Turbulent Flow and Turbulence Modeling*. Accessed: Feb. 14, 2025. Göteborg, Sweden, Jan. 2025. URL: https://www.tfd.chalmers.se/~lada/postscript_files/solids-and-fluids_turbulent-flow_turbulence-modelling.pdf.

[3] H. K. Versteeg and W. Malalasekera. *An Introduction to Computational Fluid Dynamics: The Finite Volume Method*. 2nd. Harlow, England: Pearson Education, 2007. ISBN: 978-0131274983.

[4] SimScale. *K-Epsilon Turbulence Models*. Accessed: 2025-02-19. 2023. URL: https://www.simscale.com/docs/simulation-setup/global-settings/k-epsilon/.

[5] CFD Support. *Turbulent Boundary Layer*. Accessed: 2025-02-20. 2025. URL: https://www.cfdsupport.com/openfoam-training-by-cfd-support/node342.html.

[6] Siemens PLM Software. *STAR-CCM+ User Guide: Turbulent Velocity Profile and Its Different Layers*. Accessed: 2025-02-26. 2024. URL: https://plm.sw.siemens.com/en-US/star-ccm-plus/.

[7] G.F. Hundy, A.R. Trott, and T.C. Welch. "Chapter 24 - Air Movement". In: *Refrigeration and Air-Conditioning (Fourth Edition)*. Ed. by G.F. Hundy, A.R. Trott, and T.C. Welch. Fourth Edition. Oxford: Butterworth-Heinemann, 2008, pp. 281–302. ISBN: 978-0-7506-8519-1. DOI: https://doi.org/10.1016/B978-0-7506-8519-1.00024-4. URL: https://www.sciencedirect.com/science/article/pii/B9780750685191000244.

[8] Swegon. *GOLD Luftbehandlingsaggregat*. https://www.swegon.com/sv/produkter-och-tjanster/luftbehandling/luftbehandlingsaggregat/gold/. Accessed: 2025-02-20.

[9] Swegon. *Luftbehandlingsaggregat Översikt*. Hämtad: 20 februari 2025. 2025. URL: https://www.swegon.com/siteassets/_product-documents/air-handling-units/gold-version-f/general/_sv/luftbehandlingsaggregat_oversikt2.pdf.

[10] Frank P. Bleier. *Fan Handbook: Selection, Application, and Design*. New York: McGraw-Hill, 1997, p. 640. ISBN: 0-07-005933-0.

[11] A. Kayode Coker. "Chapter 18 - Compression Equipment (Including Fans)". In: *Ludwig's Applied Process Design for Chemical and Petrochemical Plants (Fourth Edition)*. Ed. by A. Kayode Coker. Fourth Edition. Boston: Gulf Professional Publishing, 2015, pp. 729–978. ISBN: 978-0-7506-8524-5. DOI: https://doi.org/10.1016/B978-0-08-094242-1.00018-8. URL: https://www.sciencedirect.com/science/article/pii/B9780080942421000188.

[12] Air Movement and Control Association International (AMCA). *AMCA Publication 201-23: Fans and Systems*. Handbook/Manual/Guide. Air Movement and Control Association (AMCA). Arlington Heights, IL, 2023.

[13] Aerovent. *Understanding Fan Curves*. FE-2000 Fan Engineering Bulletin. Aerovent Fan Engineering. Dec. 2018. URL: https://www.aerovent.com/wp-content/uploads/2018/12/Understanding-Fan-Curves-FE-2000.pdf (visited on 06/16/2025).

[14] U.S. Department of Energy. *Air System Fans: Engineering Reference*. Accessed: 2025-02-26. 2017. URL: https://bigladdersoftware.com/epx/docs/8-4/engineering-reference/air-system-fans.html.

[15] Joel Ferziger, Milovan Perić, and Robert Street. *Computational Methods for Fluid Dynamics*. Jan. 2020. ISBN: 978-3-319-99691-2. DOI: 10.1007/978-3-319-99693-6.

[16] *ANSYS Fluent Theory Guide 2023 R1*. Available through ANSYS documentation portal. ANSYS Inc. 2023.

[17] Siemens. *STAR-CCM+ Documentation*. Accessed: Mar. 3, 2025. Available with a license. 2024.

[18] P. Gullberg and A. Tavernier. *Modeling of Closed Fans using CFD and Steady State Assumption of Fluid Flow*. Tech. rep. 2014-01-2344. SAE International, 2014. DOI: 10.4271/2014-01-2344. URL: https://doi.org/10.4271/2014-01-2344.

[19] ANSYS, Inc. *Multiple Reference Frame (MRF) Model, ANSYS Fluent Theory Guide, Release 2024R2*. Available with license. Accessed: Feb. 19, 2025. ANSYS, Inc. 2024. URL: https://ansyshelp.ansys.com/public/account/secured?returnurl=/Views/Secured/corp/v242/en/flu_th/flu_th_sec_mrf.html.

[20] R. Franzke, S. Sebben, T. Bark, et al. "Evaluation of the Multiple Reference Frame Approach for the Modelling of an Axial Cooling Fan". In: *Energies* 12.15 (2019). DOI: 10.3390/en12152934. URL: http://dx.doi.org/10.3390/en12152934.

[21] P. Zelenský, V. Zmrhal, M. Barták, et al. "Simulation-aided development of a compact local ventilation unit with the use of CFD analysis". In: *Building Simulation* 17 (2024), pp. 2233–2247. DOI: 10.1007/s12273-024-1183-9. URL: https://doi.org/10.1007/s12273-024-1183-9.

[22] Jie Geng Wei Peng Guoxiang Li and Wei Yan. "A strategy for the partition of MRF zones in axial fan simulation". In: *International Journal of Ventilation* 18.1 (2019), pp. 64–78. DOI: 10.1080/14733315.2018.1431361. eprint: https://doi.org/10.1080/14733315.2018.1431361. URL: https://doi.org/10.1080/14733315.2018.1431361.

[23] G. Bachler, H. Schiffermüller, and A. Bregant. "A Parallel Fully Implicit Sliding Mesh Method for Industrial CFD Applications". In: *Parallel Computational Fluid Dynamics 2000*. Ed. by C.B. Jenssen et al. Amsterdam: North-Holland, 2001, pp. 501–508. ISBN: 978-0-444-50673-3. DOI: https://doi.org/10.1016/B978-044450673-3/50129-9. URL: https://www.sciencedirect.com/science/article/pii/B9780444506733501299.

[24] F. Concli and C. Gorla. "Analysis of the power losses in geared transmissions - measurements and CFD calculations based on open source codes". In: *International Gear Conference 2014: 26th–28th August 2014, Lyon*. Ed. by Philippe Velex. Oxford: Chandos Publishing, 2014, pp. 1131–1140. ISBN: 978-1-78242-194-8. DOI: https://doi.org/10.1533/9781782421955.1131. URL: https://www.sciencedirect.com/science/article/pii/B9781782421948501178.

[25] Sylvester Serban Stankic and Radu-Cristian Ploesteanu. "Investigation of the Effect of Multiple Centrifugal Fans Close to Each Other in Operation – A Numerical Study to Improve Fan Efficiency in an Air Handling Unit". Master's thesis. Chalmers University of Technology, 2019. URL: https://hdl.handle.net/20.500.12380/257352.

[26] Filip Milikic. "Simulation on centrifugal fans operating at close distance: An investigation of different air handling unit constructions to improve fan efficiency". Master's thesis. Chalmers University of Technology, 2021. URL: https://hdl.handle.net/20.500.12380/302207.

[27] Siemens Digital Industries Software. *Moving Reference Frames: Rotating Fan, Simcenter STAR-CCM+ 2402 User Guide*. Accessed: Feb. 19, 2025, Available with a licence. Siemens Digital Industries Software. 2024.

[28] Linus Forsman and Lucas Hamard. “Numerical Simulation of Novel Cooling Fan Concept for BEVs. Investigation of Aerodynamic Performance of Novel Cooling Fan Concept and Comparison with Conventional Fan Concept Using Computational Fluid Dynamics”. Master’s thesis. Gothenburg, Sweden: Chalmers University of Technology, 2023. URL: http://hdl.handle.net/20.500.12380/306741.

[29] LEAP Australia. *Convergence and Mesh Independent Study*. 2025. URL: https://www.leapaust.com.au/blog/cfd/convergence-and-mesh-independent-study/ (visited on 03/11/2025).

[30] Martin Ottersten. *AIR HANDLING UNIT COMPRISING FLOW GUIDING STATOR DISC*. U.S. Patent Application US20230120245A1. Published Apr. 20, 2023. Apr. 2023.

A

Appendix

A.1 Mesh settings

Case name	Orginal	Case 1	Case 2	Case 3	Case 4	Case 5	Case 6	Case 7	Case 8
Inlet									
Base size inlet	7mm	10mm	14mm	16mm	16mm	16mm	16mm	16mm	16mm
surface growth rate inlet	1.1	1,15	1.1	1,1	1,1	1,1	1,1	1,1	1,1
volume growth rate	1.2	1.2	1.2	1.2	1.2	1.2	1.2	1.2	1.2
Part control: Maximum tetsize	8mm	8mm	14mm	16mm	16mm	16mm	16mm	16mm	16mm
inlet: surface size target	8mm	8mm	14mm	16mm	16mm	16mm	16mm	16mm	16mm
inlet: surface size min	8mm	8mm	14mm	16mm	16mm	16mm	16mm	16mm	16mm
wall-room-inlet surface target	8mm	8mm	14mm	16mm	16mm	16mm	16mm	16mm	16mm
wall-room-inlet surface min	8mm	8mm	14mm	16mm	16mm	16mm	16mm	16mm	16mm
Interface outlet, target	2mm	2mm	2mm	2mm	2mm	2mm	2mm	2mm	7mm
Interface outlet, min	2mm	2mm	2mm	2mm	2mm	2mm	2mm	2mm	7mm
Wall inlet, target	5mm	5mm	5mm	5mm	5mm	5mm	5mm	5mm	10mm
Wall inlet, min	5mm	5mm	5mm	5mm	5mm	5mm	5mm	5mm	10mm
Wall inlet II, target	1.8mm	1.8mm	1.8mm	1.8mm	1.8mm	1.8mm	1.8mm	1.8mm	5mm
Wall inlet II, min	1.8mm	1.8mm	1.8mm	1.8mm	1.8mm	1.8mm	1.8mm	1.8mm	5mm
Prism layer total thickness in all regions	3mm	3mm	3mm	3mm	3mm	3mm	3mm	3mm	3mm
Number of cells	17 055 204	15 614 307	12 591 959	10 480 359	7018792	5 868 309	4 742 277	3 786 854	1 989 815
Ratio Cells	1	91,5516%	73,8306%	61,4496%	41,1534%	34,4077%	27,8055%	22,2035%	11,6669%

Case name	Orginal	Case 1	Case 2	Case 3	Case 4	Case 5	Case 6	Case 7	Case 8
Downstream (Outlet)									
base size downstream	7mm	10mm	14mm	16mm	16mm	16mm	20mm	20mm	25mm
growth rate downstream	1.1	1.15	1.1	1.1	1.1	1.1	1.1	1.2	1.2
Volumetric control, size	3mm	4mm	5mm	6mm	6mm	6mm	10mm	10mm	12mm
Outlet surface size target.	10mm	15mm	20mm	25mm	25mm	25mm	25mm	25mm	30mm
Outlet surface size min:	10mm	10mm	20mm	25mm	25mm	25mm	25mm	25mm	30mm
wall fan assembly target:	2mm	2mm	4mm	5mm	5mm	5mm	8mm	10mm	12mm
wall fan assembly min	2mm	2mm	4mm	5mm	5mm	5mm	8mm	10mm	12mm
Part control: Maximum tetsize	8mm	8mm	14mm	16mm	16mm	16mm	20mm	25mm	25mm
Wall RO II target	5mm	5mm	5mm	8mm	8mm	8mm	12mm	14mm	16mm
Wall RO II min	5mm	5mm	5mm	8mm	8mm	8mm	12mm	14mm	16mm
Wall inlet, target size	4mm	4mm	4mm	4mm	4mm	4mm	8mm	10mm	12mm
Wall inlet, min size	4mm	4mm	4mm	4mm	4mm	4mm	8mm	10mm	12mm
Wall inlet II, target	4mm	4mm	4mm	4mm	4mm	4mm	8mm	10mm	12mm
Wall inlet II, min size	4mm	4mm	4mm	4mm	4mm	4mm	8mm	10mm	12mm
Wall shroud, target	3mm	3mm	3mm	3mm	3mm	3mm	6mm	8mm	12mm
Wall shroud, min size	3mm	3mm	3mm	3mm	3mm	3mm	6mm	8mm	12mm
Wall shroud edge, target	0.5mm	0.5mm	0.5mm	0.5mm	0.5mm	0.5mm	0.5mm	0.5mm	1.5mm
Wall shroud edge, min size	0.5mm	0.5mm	0.5mm	0.5mm	0.5mm	0.5mm	0.5mm	0.5mm	1.5mm
Wall BP, targer	4mm	4mm	4mm	4mm	4mm	4mm	4mm	4mm	12mm
Wall BP, min	4mm	4mm	4mm	4mm	4mm	4mm	4mm	4mm	12mm
Wall BP Edge, target	0.5mm	0.5mm	0.5mm	0.5mm	0.5mm	0.5mm	0.5mm	0.5mm	1.5mm
Wall BP Edge, min	0.5mm	0.5mm	0.5mm	0.5mm	0.5mm	0.5mm	0.5mm	0.5mm	1.5mm
Interface inlet, target	2mm	2mm	2mm	2mm	2mm	2mm	2mm	2mm	4mm
Interface inlet, min	2mm	2mm	2mm	2mm	2mm	2mm	2mm	2mm	4mm
Interface outlet 2, target	1mm	1mm	1mm	1mm	1mm	1mm	1mm	1mm	2mm
Interface outlet 2, min	1mm	1mm	1mm	1mm	1mm	1mm	1mm	1mm	2mm

Case name	Orginal	Case 1	Case 2	Case 3	Case 4	Case 5	Case 6	Case 7	Case 8
Fan									
base size fan	7mm	10mm	10mm	10mm	10mm	10mm	10mm	12mm	12mm
growth rate fan	1.1	1.15	1.1	1.1	1.1	1.1	1.1	1.1	1.1
Part control maximum tet size	2mm	3mm	4mm	4mm	5mm	5mm	2mm	6mm	8mm
Blade target surface	0.8mm	0.8mm	0.8mm	0.8mm	1.2mm	1.6mm	1.6mm	1.8mm	2mm
Blade minimum surface	0.8mm	0.8mm	0.8mm	0.8mm	1.6mm	1.6mm	1.6mm	1.8mm	2mm
Blade LE, target surface size	0.3mm	0.3mm	0.3mm	0.3mm	0.4mm	0.6mm	0.6mm	0.8mm	1mm
Blade LE, minimum sufr	0.3mm	0.3mm	0.3mm	0.3mm	0.4mm	0.6mm	0.6mm	0.8mm	1mm
Blade TE, target surf	0.2mm	0.2mm	0.2mm	0.2mm	0.4mm	0.4mm	0.4mm	0.6mm	1mm
Blade TE, min surf	0.2mm	0.2mm	0.2mm	0.2mm	0.4mm	0.4mm	0.4mm	0.6mm	1mm
Back plate, target	3.8mm	3.8mm	3.8mm	3.8mm	5mm	7mm	7mm	8mm	10mm
Back plate, min surf	3.8mm	3.8mm	3.8mm	3.8mm	5mm	7mm	7mm	8mm	10mm
Interface Inlet, target	2mm	2mm	2mm	2mm	4mm	5mm	3 mm	5mm	7mm
Interface Inlet, min surf	2mm	2mm	2mm	2mm	4mm	5mm	3 mm	5mm	7mm
Interface Inlet, surface growth rate	1.1	1.1	1.1	1.1	1.1	1.1	1.025	1.1	1.1
Interface Inlet_2, target	1mm	1mm	1mm	1mm	1.5mm	2mm	2 mm	2mm	2mm
Interface Inlet_2, min surf	1mm	1mm	1mm	1mm	1.5mm	2mm	2 mm	2mm	2mm
Interface Inlet_2, surface growth rate	1.1	1.1	1.1	1.1	1.1	1.1	1.025	1.025	1.025
Interface Outlet, target	2mm	2mm	2mm	2mm	3mm	4mm	2mm	4mm	4mm
Interface Outlet, min surf	2mm	2mm	2mm	2mm	3mm	4mm	2mm	4mm	4mm
Interface Outlet, surface growth rate	1.1	1.1	1.1	1.1	1.1	1.1	1.025	1.025	1.025
Shroud, target	1.6mm	1.6mm	1.6mm	1.6mm	2.5mm	3mm	2.5 mm	3.5mm	4mm
Shroud min	1.6mm	1.6mm	1.6mm	1.6mm	2.5mm	3mm	2.5 mm	3.5mm	4mm
Shroud 2, target	1.4mm	1.4mm	1.4mm	1.4mm	2mm	2.8mm	1.2 mm	3mm	4mm
Shroud 2, min	1.4mm	1.4mm	1.4mm	1.4mm	2mm	2.8mm	1.2 mm	3mm	4mm
Shroud 2, surface growth rate	1.1	1.1	1.1	1.1	1.1	1.1	1.1	1.1	1.1
Wall room fan, taget	1mm	1mm	1mm	1mm	1.5mm	2mm	1.2 mm	2mm	2mm
Wall room fan, min	1mm	1mm	1mm	1mm	1.5mm	2mm	1.2 mm	2mm	2mm
Wall room fan. surface growth rate	1.1	1.1	1.1	1.1	1.1	1.1	1.05	1.05	1.05

DEPARTMENT OF MECHANICS AND MARITIME SCIENCES
CHALMERS UNIVERSITY OF TECHNOLOGY
Gothenburg, Sweden 2025
www.chalmers.se

CHALMERS
UNIVERSITY OF TECHNOLOGY